2011-12-12

Numerical Study of Three Dimensional Low Magnetic Reynolds Number Hypersonic Magnetohydrodynamic Flows

Jaejin Lee
University of Miami, tachyian@gmail.com

UNIVERSITY OF MIAMI

NUMERICAL STUDY OF THREE DIMENSIONAL LOW MAGNETIC REYNOLDS NUMBER HYPERSONIC MAGNETOHYDRODYNAMIC FLOWS

By

Jaejin Lee

A DISSERTATION

Submitted to the Faculty
of the University of Miami
in partial fulfillment of the requirements for
the degree of Doctor of Philosophy

Coral Gables, Florida

December 2011

UNIVERSITY OF MIAMI

A dissertation submitted in partial fulfillment of
the requirements for the degree of
Doctor of Philosophy

NUMERICAL STUDY OF THREE DIMENSIONAL LOW MAGNETIC REYNOLDS NUMBER HYPERSONIC MAGNETOHYDRODYNAMIC FLOWS

Jaejin Lee

Approved:

Manuel A. Huerta, Ph.D. Professor of Physics	Terri A. Scandura, Ph.D. Dean of the Graduate School
Howard Gordon, Ph.D. Professor of Physics	GeCheng Zha, Ph.D. Professor of Mechanical & Aerospace Engineering
Kenneth Voss, Ph.D. Professor of Physics	

LEE, JAEJIN (Ph.D., Physics)
Numerical Study of Three Dimensional Low Magnetic Reynolds Number Hypersonic Magnetohydrodynamic Flows (December 2011)

Abstract of a dissertation at the University of Miami.

Dissertation supervised by Professor Manuel A. Huerta.
No. of pages in text. (78)

Hypersonic vehicles generate shocks that can heat the air sufficiently to partially ionize the air and create an electrically conducting plasma that can be studied using the equations of single fluid magnetohydrodynamics (MHD). Introducing strong applied magnetic and electric fields into the flow could have beneficial effects such as reducing heat damage, providing a sort of MHD parachute, and generating electric power or thrust in the vehicle. The Low Diffusion E-CUSP (LDE) scheme with a fifth order WENO scheme has recently been developed by Zha et al. [1, 2]. The purpose of this work is to incorporate the low magnetic Reynolds number MHD model and the thermodynamics of high temperature air to the above CFD algorithm so that it can be used to simulate hypersonic flows with MHD effects. In this work we compare results treating air as chemically frozen, neglecting all high temperature real gas effects with results obtained treating the air as a real gas in thermodynamic equilibrium, whose thermodynamic properties are changed by the high temperature. The hypersonic flows at high altitudes considered in this study have low Reynolds numbers. The Reynolds numbers range from about 2000 to 5000 for Mach 6 flows and reach up to 1.2×10^6 for Mach 15 flows. Thus, the flows are treated as laminar for the former cases and as turbulent for the latter using the Baldwin-Lomax turbulence model.

To my precious family, Young-Ah and Hansohl

Acknowledgment

I would like to thank many people who have helped and guided me during my studies.

First and foremost, I would like to thank my wife, Young-Ah, for her understanding, patience, and support during my years of study. She has always sincerely believed in me and taken care of so many things to help me keep going forward. Without her support, I simply would not have made it to this point.

I am also deeply grateful to my adviser, Dr. Manuel Huerta, for his support and advice. He has given me invaluable research opportunities and always encouraged me and respected my opinion. He has not only been an academic adviser but also guided me in numerous personal ways whenever I lost my way. I am truly indebted to him.

I also want to thank Dr. Gecheng Zha for his invaluable advice and great help with my research. Without his help and support, this work would never have been finished.

I would like to thank Marco Monti for his incredible support and friendship. He never hesitated when asked to spend long hours helping me solve many technical problems.

Last but not least, I would like to thank my committee members, Dr. Howard Gordon and Dr. Kenneth Voss, for their insights, comments, and encouragement over the course of my research.

I also thank all the other people not mentioned here for their help with this work.

Contents

List of Figures

List of Abbreviations

AoA	Angle of attack
$AUSM$	Advection upstream splitting method
$B-L$	Baldwin-Lomax 0-equation turbulence model
CFD	Computational fluid dynamics
CSD	Computational structured dynamics
$CUSP$	Convective upwind and split pressure
$ECUSP$	energy convective upwind and split pressure
FSI	Fluid-structural interaction
$GSLR$	Gauss-Seidel line relaxation
LDE	Low diffusion E-CUSP scheme
$LDFSS$	Low diffusion flux splitting scheme
LES	Large eddy simulation
$LU-SGS$	Lower-upper symmetric Gauss-Seidel
MHD	magnetohydrodynamics
MPI	Message passing interface
$MUSCL$	Monotone upstream-centered schemes for conservation laws
$RANS$	Reynolds averaged Navier-Stokes equations
$WENO$	Weighted essentially non-oscillatory scheme

List of Symbols

a_∞	speed of sound at infinity, m/s
$\mathbf{B}$, $\mathbf{B_a}$, $\mathbf{E}$	magnetic field, applied magnetic field, T, and electric field, N/C
e, e_{int}	specific energy, specific internal energy, $\mathrm{kg} \cdot \mathrm{m}^2/\mathrm{sec}^2$
J_a	Jacobian determinant
L_∞	characteristic length, m
p	pressure, N/m^2
Pr	Prandtl Number
Q, $\mathbf{Q}$, $\mathbf{q}$	magnetic interaction parameter, flux vector, and total heat flux vector
R, S, T	viscosity and heat conduction flux vector
Re, Re_m	fluid and magnetic Reynolds number
U, V, W	contravariant velocity in ξ, η, ζ directions, m/s
U_∞	free stream velocity, m/s
$\mathbf{u}$, u, v, w	fluid velocity, m/s, and x, y, z components of fluid velocity, m/s
$\mathbf{S_{MHD}}$	magnetohydrodynamic source term
T	temperature, K
γ, $\tilde{\gamma}$	ratio of specific heats
σ_e	electrical conductivity, S/m
μ	dynamic viscosity, P·s
μ_{e0}	magnetic permeability in vacuum, N/A^2
ξ, η, ζ	generalized coordinates
ρ	gas density, kg/m^3
$\tau_{i,k}$, $\bar{\bar{\tau}}$	shear stress tensor
ϕ	electric potential, V

Chapter 1

Introduction

1.1 Background

Since early 1960 when X-15, the first manned hypersonic airplane, successfully reached Mach 5, there have been many efforts to understand the aerodynamics of hypersonic flows and develop technologies to overcome many technical difficulties that arise in aerospace engineering.

One of the goals of the studies of hypersonic flows is to find ways to control them so that safer, more efficient, and more reliable hypersonic flight can be achieved. In general, there are two ways to control the flows, active and passive flow controls. Regarding active flow controls, one idea is to utilize the fact that hypersonic flows can have a partially ionized region around the body. Once the characteristics of this ionized region are understood there are many ways to control the flows by applying electromagnetic forces to this region. These types of flow controls are collectively called magnetohydrodynamic flow control. It is well known that it is practically impossible to obtain an analytical solution to the general Navier-Stokes equation which governs fluid dynamics. Also, due to the difficulties in

performing experiments with hypersonic flows in a laboratory or in airborne systems, the use of empirical studies is very limited, too.

Another alternative to circumvent the situation is computational or numerical study. Computational fluid dynamics have been successfully applied to many different scientific and engineering disciplines for a long time since the development of digital computers. Based on how the governing equations are formulated in the numerical method, they are categorized mainly into three different methods: finite difference method, finite volume method, and finite element method. Each method has its own advantages and disadvantages depending on the problem of interest. For conservation laws such as the ones occurring in aerodynamics, the finite volume method has many advantages over the other methods. The most important property among them is that the finite volume methods automatically fulfill the conservation laws once the governing equations are written in a conservative form.

Magnetohydrodynamics (MHD) describes conducting fluids such as salt water, liquid metals, or ionized gases. Despite the fact that MHD theory is one of the most practical methods to describe plasma systems, it is hard to get analytical solutions to many problems due to its highly nonlinear properties and complex boundary conditions. Thus, computational MHD is preferred in many cases and air plasma at atmospheric pressure is one example. However, when the governing equations of MHD are written in conservation form, they are not completely hyperbolic but are rather a mixed form. This prevents computational MHD from utilizing some features of conventional computational fluid dynamics that have been developed to solve hyperbolic system with strong discontinuities such as shocks. Fortunately, regarding air plasmas in engineering applications, a few as-

sumptions can be made to simplify the description of the system so that the conventional computational fluid dynamics can be utilized to solve hypersonic flows with partially ionized regions. One of them is the so called low magnetic Reynolds number approximation, which assumes that the ionized air produced in hypersonic flow is a poor conductor and the induced current density is small enough that the induced magnetic field is much smaller than the applied magnetic field. The low magnetic Reynolds number approximation enables the original MHD equations to be reduced to the Navier-Stokes equations with MHD source terms added. With the governing equations written in this form, one can use the conventional CFD method to solve the problem of air plasmas as long as this assumption is valid. Examples of the type of systems, to which the low magnetic Reynolds number approximation can be applied, include hypersonic cruise vehicles, reentry vehicles, and the internal flow of scramjet engines.

The idea of MHD flow controls began as early as 1950s and developed through 1960s. However, due to the difficulties in obtaining analytical solutions and experimental measurements, very limited computing power to utilize numerical methods, and unavailability of strong magnets, it was not until the 1980s that various ideas of MHD flow controls could be finally studied in their own right thanks to state-of-the-art hypersonic facilities, tremendous computing power, and availability of strong superconducting magnets. A few notable original studies are considered below.

1.2 Brief Survey of Previous Research

One of the earliest studies include the theoretical calculation of hypersonic flow around a blunt body during reentry by Bush [8]. The flow was assumed to be inviscid with constant density and conductivity and confined to the stagnation region of the body. The analysis showed that the application of a magnetic field resulted in an increase in the shock standoff distance and a decrease in pressure off-axis. The result was presented in terms of the magnetic interaction parameter being defined as a ratio of Lorentz force to inertial force.

Wu [9] studied a constant viscosity, density and conductivity model for a system similar to that analyzed by Bush and showed that viscosity had an effect of decreasing the magnitude of the change in shock standoff distance.

Chuskin [10] analyzed the hypersonic flow around a magnetized sphere and cylinder using the method of integral relations and numerical techniques. The result showed an increase in shock standoff distance as Bush's result showed, but the pressure off axis also increased contrary to Bush's result.

One of the most extensive calculations was done by Porter [11]. Using a model similar to Bush's, he obtained the numerical solution for the flow field, the shock standoff, the drag coeffcient, and the pressure field. Also, the Hall effect, the viscosity effect, and finite magnetic Reynolds numbers effects were considered as well. His result showed that qualitatively similar but smaller effects as Bush's could be obtained without the Hall effect, but an increase in pressure is obtained when the Hall effect is taken into account.

There are also a limited number of experimental studies which include Ziemer [12], Seeman and Cambel [13], Nowak et al. [14], and Kranc et al. [15].

More recent studies include Bityurin [16, 17], Hoffmann [18–20], Gaitonde and Poggie [21], Fujino and Ishikawa [22], Yoshino et al. [23], and Bityurin and Bocharov [24, 25]. Most of these use advanced computational methods and some combined experimental data obtained from hypersonic wind tunnels or similar facilities. However, depending on the parameters of the flow conditions used in the research and the assumptions made by the authors in modeling the flow, not only similar generic features have been obtained but also contrary results have been reported.

1.3 Objectives

The objectives of the current research is to carry out a numerical study of hypersonic flows combined with the MHD effect using an advanced computational method to analyze the characteristics of MHD flow control and assess the applicability of such a technique to hypersonic flight. The objectives of this study can be summarized as follows: 1) Develop MHD subroutines that can be incorporated into an existing E-CUSP and WENO based numerical solver. 2) Incorporate the TGAS Simplified Curve Fit method in the new solver to treat high temperature gas effects. 3) Validate the new MHD solver. 4) Assess applicability and efficacy of MHD flow control for various atmospheric hypersonic flows.

Chapter 2

Theory

2.1 Magnetohydrodynamics

2.1.1 The MHD Model

Single-fluid magnetohydrodynamics (MHD) describes an electrically conducting but electrically neutral fluid of density ρ, velocity $\mathbf{u}$, pressure p, energy per unit mass e, viscosity tensor $\bar{\bar{\tau}}$, and heat flux vector $\mathbf{q}$. The electrical quantities are the magnetic field $\mathbf{B}$, the electric field $\mathbf{E}$, the current density $\mathbf{J}$, and the electrical conductivity σ. In principle σ should be calculated from an air chemistry model, such as in Ref. [26], but in this study it is assumed that σ is given, and the air chemistry is not considered. The plasma is taken to obey Ohm's law

$$\mathbf{J} = \sigma(\mathbf{E} + \mathbf{u} \times \mathbf{B}). \tag{2.1}$$

The magnetic field is advanced in time using Faraday's law

$$\frac{\partial \mathbf{B}}{\partial t} = -\nabla \times \mathbf{E}. \tag{2.2}$$

The Ampère-Maxwell equation, which could be used to advance **E** is

$$\mu_0 \varepsilon_0 \frac{\partial \mathbf{E}}{\partial t} = \nabla \times \mathbf{B} - \mu_0 \mathbf{J}. \tag{2.3}$$

However, MHD describes low frequency phenomena, in which the conduction current is much greater than the displacement current, that is,

$$\mathbf{J} \gg \varepsilon_0 \frac{\partial \mathbf{E}}{\partial t}. \tag{2.4}$$

The displacement current is therefore neglected and we use the pre-Maxwell equation

$$\mu_0 \mathbf{J} = \nabla \times \mathbf{B}, \tag{2.5}$$

which gives **J** in terms of **B**. This means that **E** is not advanced in time, but is obtained in terms of **B** using Eqs. [2.1] and [2.5]. As a consequence of this, MHD cannot describe the usual type of high frequency electromagnetic waves. However, MHD does describe three interesting types of waves known as the Alfvén wave and the fast and slow magneto-acoustic waves. **E** can be eliminated from Eq.(2.2) and we rewrite it as

$$\frac{\partial \mathbf{B}}{\partial t} = -\nabla \times \left(\frac{\mathbf{J}}{\sigma} - \mathbf{u} \times \mathbf{B} \right) = \nabla \times (\mathbf{u} \times \mathbf{B}) + \frac{1}{\mu_0 \sigma} \nabla^2 \mathbf{B}, \tag{2.6}$$

which is the equation that advances **B** in time, and can be written in conservation form as

$$\frac{\partial \mathbf{B}}{\partial t} + \nabla \cdot (\mathbf{u} \otimes \mathbf{B} - \mathbf{B} \otimes \mathbf{u}) = \frac{1}{\mu_0 \sigma} \nabla^2 \mathbf{B}. \tag{2.7}$$

The fluid quantities $\rho, \mathbf{u}$, and e are advanced in time using the usual conservation of mass,

$$\frac{\partial \rho}{\partial t} + \nabla \cdot (\rho \mathbf{u}) = 0, \tag{2.8}$$

conservation of momentum,

$$\frac{\partial (\rho \mathbf{u})}{\partial t} + \nabla \cdot (\rho \mathbf{u} \otimes \mathbf{u}) = -\nabla p + \nabla \cdot \bar{\bar{\tau}} + \mathbf{J} \times \mathbf{B}, \tag{2.9}$$

which now includes the magnetic force density $\mathbf{J} \times \mathbf{B}$, and finally e is advanced with the equation of conservation of energy,

$$\frac{\partial}{\partial t}(\rho e) + \nabla \cdot \Big[(\rho e + p)\mathbf{u} \Big] = -\nabla \cdot \mathbf{q} + \nabla \cdot (\bar{\bar{\tau}} \cdot \mathbf{u}) + \mathbf{E} \cdot \mathbf{J}. \tag{2.10}$$

This equation is rewritten using Eq. [2.1] as

$$\frac{\partial}{\partial t}(\rho e) + \nabla \cdot \Big[(\rho e + p)\mathbf{u} \Big] = -\nabla \cdot \mathbf{q} + \nabla \cdot (\bar{\bar{\tau}} \cdot \mathbf{u}) + \frac{J^2}{\sigma} + (\mathbf{J} \times \mathbf{B}) \cdot \mathbf{u}. \tag{2.11}$$

The system is closed by giving appropriate expressions for $e, \bar{\bar{\tau}}, \mathbf{q}$, and σ in terms of the other quantities. The specific energy e is given by

$$e = e_{int} + \frac{1}{2} u^2, \tag{2.12}$$

and the pressure is obtained using

$$e_{int} = \frac{p}{(\tilde{\gamma} - 1)\rho}, \tag{2.13}$$

where e_{int} is advanced using Eq. [2.11], and $\tilde{\gamma}$, which equals 1.4 for chemically frozen air, is calculated using Eqs. [2.19] from the curve fitting method for air in chemical and thermodynamic equilibrium. In Eqs. [2.9], [2.10] and [2.11], $\mathbf{J}$ can be eliminated using Eq. [2.1].

2.1.2 The Full MHD Model and the Low Magnetic Reynolds Number Approximation

The flow around a hypersonic vehicle causes a bow shock that heats the air enough to give it some electrical conductivity. We are interested in describing steady hypersonic flow around a vehicle that carries a magnet that applies a strong steady magnetic field $\mathbf{B}_a$ to the flow with the intention of reducing surface heating and increasing the drag force. The drag force increases because the integral of $\mathbf{J} \times \mathbf{B}$ over the fluid volume appears as a reaction force on the magnet. The vehicle may also have conductors on its surface arranged so as to generate electrical power by extracting energy from the flow. The vehicle might also have a steady source of $\mathscr{E}$mf, $\mathscr{E}_a$, and apply a strong electric field $\mathbf{E}_a$, such as in a nozzle, to produce MHD thrust.

We consider $\mathbf{B}_a$ and $\mathbf{E}_a$ as independent of time in the reference frame of the vehicle. The total magnetic and electric fields in the plasma $\mathbf{B} = \mathbf{B}_a + \mathbf{B}_i$ and $\mathbf{E} = \mathbf{E}_a + \mathbf{E}_i$ are the sum of the applied and induced fields. The applied fields have zero divergence and curl inside the flow field. The full MHD model presented in Section 2.1.1 advances in time the eight-dimensional flux vector $[\rho, \rho u, \rho v, \rho w, B_x, B_y, B_z, \rho e_t]$, where u, v, and w are the x, y, and z components of $\mathbf{u}$, using Eqs. [2.8], [2.9], [2.11], and [2.7] in conservation form. The full MHD 8-dimensional problem is conceptually clear, because only the magnetic

field is advanced in time. The current **J** is obtained from the magnetic field using Eq. [2.5]. Finally the electric field is calculated using the boundary conditions, knowing its curl from Eq. [2.2], and its divergence from requiring that Eq. [2.1] be compatible with $\nabla \cdot \mathbf{J} = 0$.

Several authors have treated the full 8-dimensional problem. For example, a nozzle problem with a generator section to extract power from the incoming flow, and an accelerator section to produce thrust, using a tensor conductivity was treated in Ref. [26]. Ref. [18] also used the full 8-dimensional MHD model to treat flows around a flat plate and around a blunt body with zero electric field. The ionized air produced in the hypersonic flow is a poor electrical conductor. Therefore the electrical current **J** induced in the plasma is small. The magnetic field $\mathbf{B}_i$ generated by the plasma current is much smaller than the applied field, and diffuses in a fast time scale, which complicates the numerical simulations. This allows the use of a low magnetic Reynolds number approximation.

When expressed in dimensionless variables, the electrical conductivity σ_e enters the problem via the magnetic Reynolds number

$$Re_m = \mu_0 \sigma_e U_{ref} L_{ref}, \tag{2.14}$$

where U_{ref} and L_{ref} are appropriate reference values of speed and length in the problem. When Re_m is small it is possible to treat the problem in a low Re_m approximation, which neglects the fields $\mathbf{B}_i$ and $\mathbf{E}_i$ induced by the plasma. In this model only the five fluid quantities in the five-dimensional flux vector $[\rho, \rho u, \rho v, \rho w, \rho e]$ need to be advanced in time using Eqs.[2.8], [2.9], and [2.11], with MHD source terms proportional to **J**. Refs. [17] - [27] used the low Re_m approximation to study interesting effects, such as the MHD parachute

and MHD power generation. MacCormack [28] showed that the full MHD solution agrees with the low Re_m solution for flow in a thrust producing nozzle for $Re_m = 0.17$. Damevin and Hoffmann [19] compared the full MHD solution including air chemistry with the low Re_m approximation in flows over a hemisphere and a cylinder. Khan, Hoffmann and Dietiker [20] used the full MHD model to treat flows with zero electric field around a flat plate and a blunt body and tested for agreement between the solutions of the full MHD model and the low Re_m approximation. They obtained good agreement for values of $Re_m < 0.125$.

2.1.3 Ohm's Law and Electrical Conductivity Models

The electrical current density $\mathbf{J}$ is calculated using a form of Ohm's law. When the Hall current and ion slip are important there appear, in addition to the ordinary scalar electrical conductivity of the electrons, σ_e, a Hall conductivity σ_H and a perpendicular conductivity $\sigma_\perp$. These involve the electron and ion Hall parameters β_e and β_i, and the ion slip factor $s = \beta_e\beta_i$. The Hall parameters are given by

$$\beta_e = \frac{\omega_e}{\bar{\nu}_e}, \quad \text{and} \quad \beta_i = \frac{\omega_i}{\bar{\nu}_i}, \tag{2.15}$$

where ω_e and ω_i are the electron and ion Larmor frequencies, and $\bar{\nu}_e$ and $\bar{\nu}_i$ are the effective electron and ion collision frequencies. As discussed in Sutton and Sherman [29] and using the notation in [26], $\sigma_\perp$ and σ_H are given by

$$\sigma_\perp = \frac{1+s}{(1+s)^2+\beta_e^2}\sigma_e, \text{ and } \sigma_H = \frac{\beta_e}{(1+s)^2+\beta_e^2}\sigma_e, \text{ which give } \sigma_\perp \approx \sigma_H \approx \frac{\sigma_e}{\beta_e} \text{ for large } \beta_e. \tag{2.16}$$

Due to the strong magnetic fields and low densities in our simulations we estimate that β_e is large, of the order of 10^3, and β_i is of order 1. We see from Eq.2.16 that in our case $\sigma_\perp$ and σ_H are much smaller than σ_e. Therefore we neglect effects like Hall current and ion slip, which greatly simplifies our simulations, and we calculate the current density with the ordinary electrical conductivity using the simple Ohm's law of Eq. 2.1. We consider simple models for σ_e. The so called equilibrium ionization model assumes the electrical conductivity of the air is a constant throughout the entire shock layer [21] and zero elsewhere:

$$\sigma_e = \begin{cases} \sigma_{e,ref} & \text{inside shock layer} \\ 0 & \text{elsewhere,} \end{cases} \tag{2.17}$$

where $\sigma_{e,ref}$ is the reference electrical conductivity. However, considering the temperature variation in the shock layer this assumption is not well justified because σ_e depends strongly on the temperature. Other authors, such as in Refs. [30] and [21], consider a better variable electrical conductivity model based on a power-law.

Because the simple power law model tends to exaggerate the conductivity we modify this by introducing an onset temperature

$$\sigma_e = \sigma_{e,ref}\Theta(\mathrm{T} - \mathrm{T_{onset}}) \left(\frac{\mathrm{T}}{\mathrm{T_0}}\right)^{\mathrm{k}} \tag{2.18}$$

where Θ is the Heaviside step function, $\mathrm{T_{onset}}$ is the onset temperature, $\mathrm{T_0}$ is the stagnation temperature, and k is the exponent of the power-law model. We call this power-law-onset model.

The physical conditions we consider are similar to those in Ref. [27], so we take $\sigma_{e,ref} = 100\,\mathrm{S/m}$ as the reference electrical conductivity, which is representative of the

more rigorous results of Ref. [27]. The results for $T_{onset} = 4000K$ and $T_{onset} = 6000K$ are compared in Fig. [9.12]. Also, the results with k=1, 2, and 3, which are called P1, P2, and P3 respectively, are compared in Fig. [9.5].

2.2 Atmospheric Hypersonic Flows

Although there is no clear cut as to where hypersonic flow regime starts, a flow is usually considered as hypersonic if the speed of the flow exceeds about Mach 5.

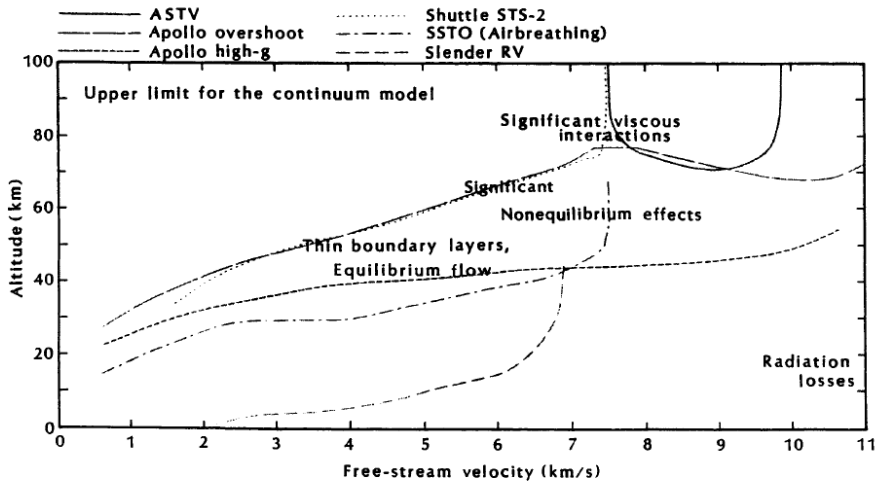

Figure 2.1: Velocity/Altitude parameters for several reentry vehicles, as taken from Bertin [5].

Fig. [2.1] shows a few examples of the flight paths of hypersonic vehicles. The characteristics of different flow regimes experienced by some of the hypersonic vehicles in the previous figure are summarized in Fig.[2.2]. In the hypersonic flow regime many phenom-

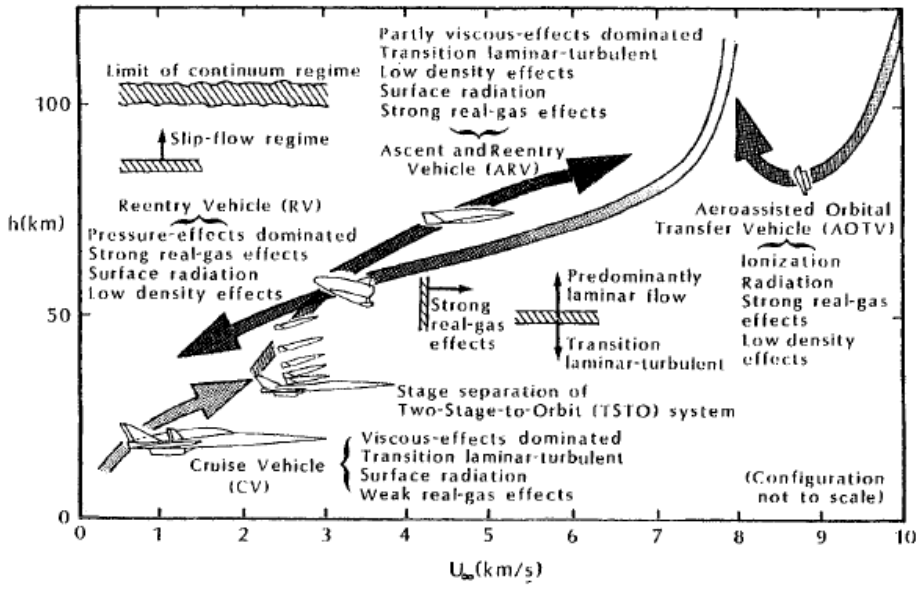

Figure 2.2: Four major classes of hypersonic space-transport vehicles, and major aerothermodynamics effects, as taken from Hirschel [6].

ena start to develop and these make the flow differ from supersonic flow. One of the basic characteristics of hypersonic flow is its thin shock layer compared with supersonic flow. As the Mach number increases the attached shock gets very close to the surface of the body and extreme conditions develop inside the shock layer. The viscosity coefficient increases with temperature. When the flow inside the shock layer slows down, a large amount of kinetic energy is transformed into internal energy. This process makes the temperature in the boundary layer increase and in turn the viscosity coefficient increases. In addition, because the pressure in the normal direction through a boundary layer is constant, the in-

crease in temperature makes the density decrease. As a result, to conserve the mass passing through the boundary layer, the thickness of the boundary layer increases. Combined with an increased viscosity coefficient itself inside the boundary layer, this makes the boundary layer grow rapidly. This thickened boundary layer interacts with the inviscid region of the shock layer and changes the inviscid region and vice versa. This phenomenon is called viscous interaction.

The extremely high temperature of hypersonic flow can cause excitation of the vibrational energy of air molecules and triggers dissociation of molecules and eventually ionization of gas. The conditions for this process depends on the altitude. Fig. [2.3] shows

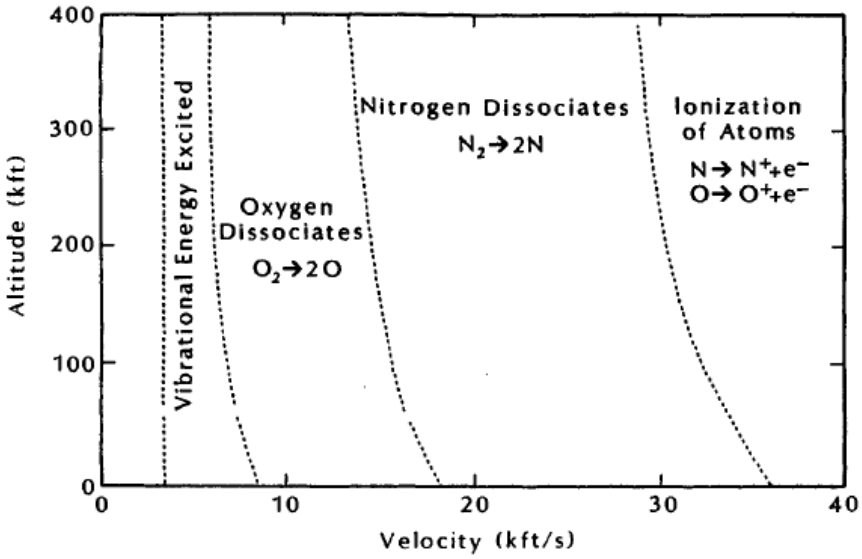

Figure 2.3: Dominant chemical reactions for equilibrium air in the stagnation region, as taken from Hansen and Heims [7].

dominant chemical reactions on altitude-velocity map for equilibrium air. For air at 1 atm pressure, the oxygen molecules start to dissociate at about 2000K and are completely

dissociated at about 4000K, where the dissociation of the nitrogen molecules starts. At about 9000K the nitrogen molecules completely dissociate, and above this temperature the ionization process begins and the air becomes a partially ionized gas.

2.2.1 Treatment of High Temperature Gas Effects

The high temperature behind the hypersonic bow shock causes molecular dissociation, chemical reactions, ionization, and other effects that change the equation of state and the energy equation of the gas. A complete treatment of this requires the inclusion of reaction rate equations for each chemical species, the inclusion of rotational and vibrational energy equations, and other effects, possibly with the presence of two or even three distinct temperatures.

Based on particle densities and collision cross sections we estimate that the molecular collision times are $\sim 10^{-7} - 10^{-8}$ s. In flow regions where the transit time of the air is much larger than the molecular collision time, local thermodynamic equilibrium may develop. In the cases considered in this study the free stream speeds are $\sim 5 \times 10^3$ m/s, and the shock stand-off distances are ~ 0.08 m. The transit time of the air over the shock stand-off distance is then $\sim 1.6 \times 10^{-5}$ s, which is much longer than the collision time. Therefore, air in chemical and thermodynamic equilibrium is treated using the curve fit method implemented in the TGAS FORTRAN subroutines developed by Srinivasan, Tannehill, and Weilmuenster [31], and Srinivasan, Tannehill, and Weilmuenster [32]. These subroutines are good for temperatures up to $T = 25,000$ K, and particle density from 10^{-7} to 10^3 times 2.687×10^{25} 1/m^3, which is the particle density of an ideal gas at a pressure of 1 atm and a temperature of 273.15 K. The authors mention that the subroutines apply

to air, and other gas mixtures, and include molecular rotation, vibration, dissociation, and ionization.

The TGAS subroutines give the pressure p and temperature T in terms of an equivalent ratio of specific heats $\tilde{\gamma}$ in the form

$$\tilde{\gamma} = \tilde{\gamma}(e_{int}, \rho), \quad p = \rho e_{int}(\tilde{\gamma} - 1), \quad T = T(p, \rho), \tag{2.19}$$

where ρ and e_{int} are the gas density and specific internal energy.

2.2.2 Baldwin-Lomax Turbulence Model

The flow conditions used in this study are mostly low density due to the high altitude which make the Reynolds number small enough so that the flows can be treated as laminar flows. However, some cases have large Reynolds number due to very high speed and relatively large characteristic size and require turbulence modeling. The Baldwin-Lomax turbulece model was first proposed in Baldwin and Lomax [33]. It is an eddy viscosity model which simply adds an additional term to the transport coefficients without solving any additional equations. In all viscous flow equations, the viscosity μ is replaced by $(\mu + \mu_T)$ and the thermal conductivity k is replaced by $(k + k_T)$ where μ_T and k are the eddy viscosity and the eddy thermal conductivity, respectively. It is known to yield reasonable results for a wide range of Mach numbers from subsonic to hypersonic. This model treats the boundary layer as two split layers, an inner and an outer layer, each layer being described

by the following turbulence viscosity:

$$\mu_T = \begin{cases} (\mu_T)_{inner} & y \leq y_{crossover} \\ (\mu_T)_{outer} & y \geq y_{crossover} \end{cases} \tag{2.20}$$

where y is the local normal distance from the wall, and $y_{crossover}$ is the crossover point from the inner to the outer layer. For the inner layer,

$$(\mu_T)_{inner} = \rho l^2 |\omega| \tag{2.21}$$

where

$$l = ky\left[1 - \exp\left(\frac{-y^+}{A^+}\right)\right], \qquad y^+ = \frac{\sqrt{\rho_w \tau_w} y}{\mu_w} \tag{2.22}$$

and k and A^+ are two dimensionless constants to be specified. Here, ω is the local vorticity and is defined, for example, for a two dimensional flow as

$$\omega = \frac{\partial u}{\partial y} - \frac{\partial v}{\partial x}. \tag{2.23}$$

For the outer layer,

$$(\mu_T)_{outer} = \rho K C_{cp} F_{wake} F_{Kleb} \tag{2.24}$$

where K and C_{cp} are two additional constants, and F_{wake} and F_{Kleb} are related to the function

$$f(y) = y|\omega|\left[1 - \exp\left(\frac{-y^+}{A^+}\right)\right]. \tag{2.25}$$

$f(y)$ will have a maximum value along a given normal distance y. This maximum value and the location it occurs are denoted by F_{max} and y_{max}, respectively. In Eq. [2.24], $F_{wake} = \min[y_{max}F_{max}, C_{wk}y_{max}U_{dif}^2/Fmax]$ where C_{wk} is constant and $U_{dif} = \sqrt{u^2+v^2}$, and

$$F_{Kleb}(y) = \left[1 + 5.5\left(C_{Kleb}\frac{y}{y_{max}}\right)^6\right]^{-1}. \tag{2.26}$$

Thus, there are six constants in the model and they are: $A^+ = 26.0, C_{cp} = 1.6, C_{Kleb} = 0.3, C_{wk} = 0.25, k = 0.4, K = 0.0168$.

Chapter 3

Governing Equations

3.1 3D Navier-Stokes Equations

The governing equations are the spatially filtered compressible Navier-Stokes equations. The spatial filtering removes the small scale high frequency components of the fluid motion, while keeping the unsteadiness associated with the large scale turbulent motion. Following the derivation of Knight et al. [34], the filtered compressible Navier-Stokes equations in Cartesian coordinates can be expressed as:

$$\frac{\partial \mathbf{Q}}{\partial t} + \frac{\partial \mathbf{E}}{\partial x} + \frac{\partial \mathbf{F}}{\partial y} + \frac{\partial \mathbf{G}}{\partial z} = \frac{1}{Re}\left(\frac{\partial \mathbf{E_v}}{\partial x} + \frac{\partial \mathbf{F_v}}{\partial y} + \frac{\partial \mathbf{G_v}}{\partial z}\right) \tag{3.1}$$

where t is time, Re is the Reynolds number. The variable vector $\mathbf{Q}$, inviscid flux vectors $\mathbf{E}$, $\mathbf{F}$, $\mathbf{G}$, and the viscous fluxes $\mathbf{E_v}$, $\mathbf{F_v}$, $\mathbf{G_v}$ are given as the following.

$$\mathbf{Q}=\begin{pmatrix}\bar{\rho}\\ \bar{\rho}\tilde{u}\\ \bar{\rho}\tilde{v}\\ \bar{\rho}\tilde{w}\\ \bar{\rho}\tilde{e}\end{pmatrix},\ \mathbf{E}=\begin{pmatrix}\bar{\rho}\tilde{u}\\ \bar{\rho}\tilde{u}^2+\bar{p}\\ \bar{\rho}\tilde{u}\tilde{v}\\ \bar{\rho}\tilde{u}\tilde{w}\\ (\bar{\rho}\tilde{e}+\bar{p})\tilde{u}\end{pmatrix},\ \mathbf{F}=\begin{pmatrix}\bar{\rho}\tilde{v}\\ \bar{\rho}\tilde{v}\tilde{u}\\ \bar{\rho}\tilde{v}^2+\bar{p}\\ \bar{\rho}\tilde{v}\tilde{w}\\ (\bar{\rho}\tilde{e}+\bar{p})\tilde{v}\end{pmatrix},\ \mathbf{G}=\begin{pmatrix}\bar{\rho}\tilde{w}\\ \bar{\rho}\tilde{w}\tilde{u}\\ \bar{\rho}\tilde{w}\tilde{v}\\ \bar{\rho}\tilde{w}^2+\bar{p}\\ (\bar{\rho}\tilde{e}+\bar{p})\tilde{w}\end{pmatrix} \tag{3.2}$$

$$\mathbf{E_v}=\begin{pmatrix}0\\ \bar{\tau}_{xx}+\sigma_{xx}\\ \bar{\tau}_{xy}+\sigma_{xy}\\ \bar{\tau}_{xz}+\sigma_{xz}\\ Q_x\end{pmatrix},\ \mathbf{F_v}=\begin{pmatrix}0\\ \bar{\tau}_{yx}+\sigma_{yx}\\ \bar{\tau}_{yy}+\sigma_{yy}\\ \bar{\tau}_{yz}+\sigma_{yz}\\ Q_y\end{pmatrix},\ \mathbf{G_v}=\begin{pmatrix}0\\ \bar{\tau}_{zx}+\sigma_{zx}\\ \bar{\tau}_{zy}+\sigma_{zy}\\ \bar{\tau}_{zz}+\sigma_{zz}\\ Q_z\end{pmatrix} \tag{3.3}$$

The overbar denotes a regular filtered variable, and the tilde is used to denote the Favre filtered variable. In the above equations, ρ is the density, u,v,w are the Cartesian velocity components in x,y,z directions, p is the static pressure, and e is the total energy per unit mass. The $\bar{\tau}$ is the molecular viscous stress tensor and is estimated as:

$$\bar{\tau}_{ij}=-\frac{2}{3}\tilde{\mu}\frac{\partial\tilde{u}_k}{\partial x_k}\delta_{ij}+\tilde{\mu}(\frac{\partial\tilde{u}_i}{\partial x_j}+\frac{\partial\tilde{u}_j}{\partial x_i}),\qquad i,j=1,2,3. \tag{3.4}$$

The above equation is in tensor form, where the subscripts 1, 2, 3 represent the coordinates, x,y,z, and the Einstein summation convention is used. The molecular viscosity $\tilde{\mu}=\tilde{\mu}(\tilde{T})$ is determined by the Sutherland law. The σ is the subgrid scale stress tensor due to the

filtering process and is expressed as:

$$\sigma_{ij} = -\bar{\rho}(\widetilde{u_i u_j} - \tilde{u}_i \tilde{u}_j) \tag{3.5}$$

The energy flux Q is expressed as:

$$Q_i = \tilde{u}_j(\bar{\tau}_{ij} + \sigma_{ij}) - \bar{q}_i + \Phi_i, \tag{3.6}$$

where Φ is the subscale heat flux:

$$\Phi_i = -C_p \bar{\rho}(\widetilde{u_i T} - \tilde{u}_i \tilde{T}). \tag{3.7}$$

The $\bar{q}_i$ is the molecular heat flux:

$$\bar{q}_i = -\frac{C_p \tilde{\mu}}{Pr} \frac{\partial \tilde{T}}{\partial x_i} \tag{3.8}$$

$$\bar{\rho}\tilde{e} = \frac{\bar{p}}{(\gamma - 1)} + \frac{1}{2}\bar{\rho}(\tilde{u}^2 + \tilde{v}^2 + \tilde{w}^2) + \rho k, \tag{3.9}$$

where γ is the ratio of specific heats, ρk is the subscale kinetic energy per unit volume.

$$\rho k = \frac{1}{2}\bar{\rho}(\widetilde{u_i u_i} - \tilde{u}_i \tilde{u}_i) = -\frac{1}{2}\sigma_{ii} \tag{3.10}$$

In the present calculation, the ρk in Eq.(3.9) is omitted based on the assumption that the effect is small.

In generalized coordinates, Eq.(3.1) can be expressed as the following:

$$\frac{\partial \mathbf{Q}'}{\partial t} + \frac{\partial \mathbf{E}'}{\partial \xi} + \frac{\partial \mathbf{F}'}{\partial \eta} + \frac{\partial \mathbf{G}'}{\partial \zeta} = \frac{1}{\mathrm{Re}} \left(\frac{\partial \mathbf{E}'_{\mathbf{v}}}{\partial \xi} + \frac{\partial \mathbf{F}'_{\mathbf{v}}}{\partial \eta} + \frac{\partial \mathbf{G}'_{\mathbf{v}}}{\partial \zeta} \right) \tag{3.11}$$

where

$$\mathbf{Q}' = \frac{\mathbf{Q}}{J} \tag{3.12}$$

$$\mathbf{E}' = \frac{1}{J}(\xi_t \mathbf{Q} + \xi_x \mathbf{E} + \xi_y \mathbf{F} + \xi_z \mathbf{G}) \tag{3.13}$$

$$\mathbf{F}' = \frac{1}{J}(\eta_t \mathbf{Q} + \eta_x \mathbf{E} + \eta_y \mathbf{F} + \eta_z \mathbf{G}) \tag{3.14}$$

$$\mathbf{G}' = \frac{1}{J}(\zeta_t \mathbf{Q} + \zeta_x \mathbf{E} + \zeta_y \mathbf{F} + \zeta_z \mathbf{G}) \tag{3.15}$$

$$\mathbf{E}'_{\mathbf{v}} = \frac{1}{J}(\xi_x \mathbf{E}_{\mathbf{v}} + \xi_y \mathbf{F}_{\mathbf{v}} + \xi_z \mathbf{G}_{\mathbf{v}}) \tag{3.16}$$

$$\mathbf{F}'_{\mathbf{v}} = \frac{1}{J}(\eta_x \mathbf{E}_{\mathbf{v}} + \eta_y \mathbf{F}_{\mathbf{v}} + \eta_z \mathbf{G}_{\mathbf{v}}) \tag{3.17}$$

$$\mathbf{G}'_{\mathbf{v}} = \frac{1}{J}(\zeta_x \mathbf{E}_{\mathbf{v}} + \zeta_y \mathbf{F}_{\mathbf{v}} + \zeta_z \mathbf{G}_{\mathbf{v}}) \tag{3.18}$$

where J is the transformation Jacobian. The inviscid fluxes in the generalized coordinate system are expressed as:

$$\mathbf{E}' = \begin{bmatrix} \bar{\rho}U \\ \bar{\rho}\tilde{u}U + l_x\bar{p} \\ \bar{\rho}\tilde{v}U + l_y\bar{p} \\ \bar{\rho}\tilde{w}U + l_z\bar{p} \\ (\bar{\rho}\tilde{e} + \bar{p})U - l_t\bar{p} \end{bmatrix}, \mathbf{F}' = \begin{bmatrix} \bar{\rho}V \\ \bar{\rho}\tilde{u}V + m_x\bar{p} \\ \bar{\rho}\tilde{v}V + m_y\bar{p} \\ \bar{\rho}\tilde{w}V + m_z\bar{p} \\ (\bar{\rho}\tilde{e} + \bar{p})V - m_t\bar{p} \end{bmatrix}, \mathbf{G}' = \begin{bmatrix} \bar{\rho}W \\ \bar{\rho}\tilde{u}W + n_x\bar{p} \\ \bar{\rho}\tilde{v}W + n_y\bar{p} \\ \bar{\rho}\tilde{w}W + n_z\bar{p} \\ (\bar{\rho}\tilde{e} + \bar{p})W - n_t\bar{p} \end{bmatrix}$$

where U, V and W are the contravariant velocities in ξ, η and ζ directions.

$$\begin{aligned} U &= l_t + \mathbf{l} \bullet \mathbf{V} = l_t + l_x\tilde{u} + l_y\tilde{v} + l_z\tilde{w} \\ V &= m_t + \mathbf{m} \bullet \mathbf{V} = m_t + m_x\tilde{u} + m_y\tilde{v} + m_z\tilde{w} \\ W &= n_t + \mathbf{n} \bullet \mathbf{V} = n_t + n_x\tilde{u} + n_y\tilde{v} + n_z\tilde{w} \end{aligned} \tag{3.19}$$

$\mathbf{l}$, $\mathbf{m}$, $\mathbf{n}$ are the normal vectors on ξ, η, ζ surfaces with their magnitudes equal to the elemental surface area and pointing to the directions of increasing ξ, η, ζ.

$$\mathbf{l} = \frac{\nabla\xi}{J},\ \mathbf{m} = \frac{\nabla\eta}{J},\ \mathbf{n} = \frac{\nabla\zeta}{J} \tag{3.20}$$

$$l_t = \frac{\xi_t}{J},\ m_t = \frac{\eta_t}{J},\ n_t = \frac{\zeta_t}{J}. \tag{3.21}$$

For simplicity, all the overbars and tildes in the above equations will be dropped in the rest of this thesis. Please note that the Navier-Stokes equations, Eq.(3.11), are normalized based on a set of reference parameters. The detailed normalization procedure can be found in [4].

Chapter 4

The Numerical Method

The original numerical method on which this study is based is exactly the same as used in Wang [35]. Thus, in order to describe the original numerical method as precisely as possible, most of the following is excerpted from Wang [35].

In this chapter, the numerical methods used to discretize the governing equations are introduced. The flow governing equations are discretized using the finite difference method in a fully implicit manner. The inviscid fluxes are discretized using a newly developed, low diffusion E-CUSP scheme [1, 36]. The fifth-order WENO scheme [3] is used to reconstruct the conservative variables at volume interfaces. A set of fully conservative fourth-order accurate finite central differencing scheme for the viscous terms is employed in this research [3]. These central differencing schemes are constructed so that the stencil widths are within the one of the WENO scheme. The structure governing equations are discretized and solved implicitly in the same manner, to be consistent with the flow governing equations.

4.1 Finite Difference Discretization Using Implicit Method

The 3D Navier-Stokes equations (3.1) are discretized based on conservative finite differencing, which is implemented by shifting the solution points a half grid interval in each direction on the computational domain. The solution points are hence located in the centroids of the grid cells in the computational domain (not physical domain). This makes it possible to use the same code structure of a 2nd order finite volume method. The derivative of a flux is discretized by a finite difference method. Taking inviscid flux $\mathbf{E}$ as an example, the discretized conservative form of its derivative can be written as the following

$$\frac{\partial \mathbf{E}}{\partial \xi}|_i = \frac{\mathbf{E}_{i+1/2} - \mathbf{E}_{i-1/2}}{\Delta \xi}, \tag{4.1}$$

where the inter index denotes the centroid of a cell and the half integer indices denote interfaces of the cells. Since $\Delta\xi = 1, \Delta\eta = 1, \Delta\zeta = 1$ are used in the generalized coordinate, the governing Eqs.(3.1) can be written as the following implicit form:

$$\begin{aligned}\frac{1}{\Delta t}\left(Q^{n+1} - Q^n\right) + \left(\mathbf{E}_{i+\frac{1}{2}} - \mathbf{E}_{i-\frac{1}{2}}\right)^{n+1} + \left(\mathbf{F}_{j+\frac{1}{2}} - \mathbf{F}_{j-\frac{1}{2}}\right)^{n+1} + \left(\mathbf{G}_{k+\frac{1}{2}} - \mathbf{G}_{k-\frac{1}{2}}\right)^{n+1} \\ = \left(\mathbf{R}_{i+\frac{1}{2}} - \mathbf{R}_{i-\frac{1}{2}}\right)^{n+1} + \left(\mathbf{S}_{j+\frac{1}{2}} - \mathbf{S}_{j-\frac{1}{2}}\right)^{n+1} + \left(\mathbf{T}_{k+\frac{1}{2}} - \mathbf{T}_{k-\frac{1}{2}}\right)^{n+1} + D^n\end{aligned} \tag{4.2}$$

where n and $n+1$ are two sequential time levels, which have a time interval of Δt. The 5th order WENO scheme with an upwind scheme Riemann solver is used for reconstructing inviscid fluxes $\mathbf{E}_{i+\frac{1}{2}}$, $\mathbf{F}_{j+\frac{1}{2}}$ and $\mathbf{G}_{k+\frac{1}{2}}$. A fully conservative 4th order central differencing scheme is used to evaluate the viscous fluxes R, S, T.

4.2 The Low Diffusion E-CUSP (LDE) Scheme [2]

The basic idea of the LDE scheme is to split the inviscid flux into the convective flux E^c and the pressure flux E^p. In the generalized coordinate system, the flux $\mathbf{E}$ can be split as the following:

$$\mathbf{E} = E^c + E^p = \begin{pmatrix} \rho U \\ \rho u U \\ \rho v U \\ \rho w U \\ \rho e U \\ \rho \tilde{\nu} U \end{pmatrix} + \begin{pmatrix} 0 \\ l_x p \\ l_y p \\ l_z p \\ p\overline{U} \\ 0 \end{pmatrix} \tag{4.3}$$

where, U is the contravariant velocity in ξ direction and is defined as the following

$$U = l_t + l_x u + l_y v + l_z w. \tag{4.4}$$

$\overline{U}$ is defined as:

$$\overline{U} = l_x u + l_y v + l_z w. \tag{4.5}$$

The convective term, E^c is evaluated by

$$E^c = \rho U \begin{pmatrix} 1 \\ u \\ v \\ w \\ e \\ \tilde{\nu} \end{pmatrix} = \rho U f^c,\ f^c = \begin{pmatrix} 1 \\ u \\ v \\ w \\ e \\ \tilde{\nu} \end{pmatrix}. \tag{4.6}$$

Let

$$C = c\left(l_x^2 + l_y^2 + l_z^2\right)^{\frac{1}{2}} \tag{4.7}$$

where $c = \sqrt{\gamma RT}$ is the speed of sound. Then the convective flux at interface $i + \frac{1}{2}$ is evaluated as:

$$E^c_{i+\frac{1}{2}} = C_{\frac{1}{2}}\left[\rho_L C^+ f^c_L + \rho_R C^- f^c_R\right] \tag{4.8}$$

where, the subscripts L and R represent the left and right hand sides of the interface.

$$
\begin{aligned}
&C_{\frac{1}{2}} = \tfrac{1}{2}\left(C_L + C_R\right),\ C^{+} = \alpha_L^{+}\left(1+\beta_L\right)M_L - \beta_L M_L^{+} - M_{\frac{1}{2}}^{+} \\
&C^{-} = \alpha_R^{-}\left(1+\beta_R\right)M_R - \beta_R M_R^{-} + M_{\frac{1}{2}}^{-} \\
&M_L = \tfrac{U_L}{C_{\frac{1}{2}}},\ M_R = \tfrac{U_R}{C_{\frac{1}{2}}} \\
&\alpha_{L,R} = \tfrac{1}{2}\left[1 \pm sign\left(M_{L,R}\right)\right] \\
&\beta_{L,R} = -max\left[0, 1 - int\left(\left|M_{L,R}\right|\right)\right] \\
&M_{\frac{1}{2}}^{+} = M_{\frac{1}{2}}\tfrac{C_R + C_L\Phi}{C_R + C_L},\ M_{\frac{1}{2}}^{-} = M_{\frac{1}{2}}\tfrac{C_L + C_R\Phi^{-1}}{C_R + C_L},\ \Phi = \tfrac{\left(\rho C^2\right)_R}{\left(\rho C^2\right)_L} \\
&M_{\frac{1}{2}} = \beta_L\delta^{+}M_L^{-} - \beta_R\delta^{-}M_R^{+} \\
&M_{L,R}^{\pm} = \pm\tfrac{1}{4}\left(M_{L,R} \pm 1\right)^2 \\
&\delta^{\pm} = \tfrac{1}{2}\left\{1 \pm sign\left[\tfrac{1}{2}\left(M_L + M_R\right)\right]\right\}
\end{aligned}
\qquad . \tag{4.9}
$$

The pressure flux, E^p is evaluated as the following

$$
E_{i+\frac{1}{2}}^{p} = \begin{pmatrix} 0 \\ \mathscr{P}^{+} p\, l_x \\ \mathscr{P}^{+} p\, l_y \\ \mathscr{P}^{+} p\, l_z \\ \frac{1}{2} p\left[\overline{U} + \overline{C}_{\frac{1}{2}}\right] \\ 0 \end{pmatrix}_L + \begin{pmatrix} 0 \\ \mathscr{P}^{-} p\, l_x \\ \mathscr{P}^{-} p\, l_y \\ \mathscr{P}^{-} p\, l_z \\ \frac{1}{2} p\left[\overline{U} - \overline{C}_{\frac{1}{2}}\right] \\ 0 \end{pmatrix}_R . \tag{4.10}
$$

The contravariant speed of sound $\overline{C}$ in the pressure splitting of energy equation is consistent with $\overline{U}$. It is computed based on C as the following,

$$
\overline{C} = C - l_t \tag{4.11}
$$

The use of $\overline{U}$ and $\overline{C}$ instead of U and C in the pressure splitting of energy is to take into account the grid speed so that the flux will transit from subsonic to supersonic smoothly. When the grid is stationary, as in this thesis, $l_t = 0, \overline{C} = C, \overline{U} = U$.

The pressure splitting coefficient is:

$$\mathscr{P}^{\pm}_{L,R} = \frac{1}{4}\left(M_{L,R} \pm 1\right)^2 \left(2 \mp M_L\right) \tag{4.12}$$

The LDE scheme can capture crisp shock profiles and exact contact surface discontinuities. Since the scheme uses scalar dissipation, for DES with one extra equation, the splitting is basically the same as the original scheme. This is an advantage over the Roe scheme, for which the eigenvectors need to be derived when any extra equation is added to the governing equations. It is also more computationally efficient than the Roe scheme as it has no matrix operations.

4.3 The Fifth-Order WENO Scheme [3]

The interface flux, $E_{i+\frac{1}{2}} = E(Q_L, Q_R)$, is evaluated by determining the conservative variables Q_L and Q_R using fifth-order WENO scheme [3]. For example,

$$(Q_L)_{i+\frac{1}{2}} = \omega_0 q_0 + \omega_1 q_1 + \omega_2 q_2 \tag{4.13}$$

where

$$
\begin{aligned}
q_0 &= \tfrac{1}{3}Q_{i-2} - \tfrac{7}{6}Q_{i-1} + \tfrac{11}{6}Q_i \\
q_1 &= -\tfrac{1}{6}Q_{i-1} + \tfrac{5}{6}Q_i + \tfrac{1}{3}Q_{i+1} \\
q_2 &= \tfrac{1}{3}Q_i + \tfrac{5}{6}Q_{i+1} - \tfrac{1}{6}Q_{i+2}
\end{aligned}
\tag{4.14}
$$

$$
\omega_k = \frac{\alpha_k}{\alpha_0 + \ldots + \alpha_{r-1}} \tag{4.15}
$$

$$
\begin{aligned}
&\alpha_k = \tfrac{C_k}{\varepsilon + IS_k},\ k = 0, \ldots, r-1 \\
&C_0 = 0.1,\ C_1 = 0.6,\ C_2 = 0.3 \\
&IS_0 = \tfrac{13}{12}\left(Q_{i-2} - 2Q_{i-1} + Q_i\right)^2 + \tfrac{1}{4}\left(Q_{i-2} - 4Q_{i-1} + 3Q_i\right)^2 \\
&IS_1 = \tfrac{13}{12}\left(Q_{i-1} - 2Q_i + Q_{i+1}\right)^2 + \tfrac{1}{4}\left(Q_{i-1} - Q_{i+1}\right)^2 \\
&IS_2 = \tfrac{13}{12}\left(Q_i - 2Q_{i+1} + Q_{i+2}\right)^2 + \tfrac{1}{4}\left(3Q_i - 4Q_{i+1} + Q_{i+2}\right)^2
\end{aligned}
\tag{4.16}
$$

where, ε is originally introduced to avoid the denominator becoming zero and is supposed to be a very small number. In [3], it is observed that IS_k will oscillate if ε is small and also shift the weights away from the optimum values in the smooth region. The higher the ε values, the closer the weights approach the optimum weights, C_k, which will give the symmetric evaluation of the interface flux with minimum numerical dissipation. When there are shocks in the flow field, ε can not be too large to maintain the sensitivity to shocks. In [3], the optimized value of $\varepsilon = 10^{-2}$ is recommended for the transonic flow with shock waves.

4.4 Implicit Time Integration

4.4.1 Implicit Flow Solver

The time dependent governing equations are solved using a dual time stepping method suggested by Jameson [37]. To achieve high convergence rate, the implicit pseudo time marching scheme is used with the unfactored Gauss-Seidel line relaxation. The physical temporal term is discretized implicitly using a three point, backward differencing as the following (The prime is omitted hereafter for simplicity):

$$\frac{\partial Q}{\partial t} = \frac{3Q^{n+1} - 4Q^n + Q^{n-1}}{2\Delta t} \tag{4.17}$$

where $n-1$, n and $n+1$ are three sequential time levels, which have a time interval of Δt. The first-order Euler scheme is used to discretize the pseudo temporal term to enhance diagonal dominance. The semi-discretized equations of the governing equations are finally given as the following:

$$\left[\left(\frac{1}{\Delta\tau} + \frac{1.5}{\Delta t}\right) I - \left(\frac{\partial R}{\partial Q}\right)^{n+1,m}\right] \delta Q^{n+1,m+1} = R^{n+1,m} - \frac{3Q^{n+1,m} - 4Q^n + Q^{n-1}}{2\Delta t} \tag{4.18}$$

where the $\Delta\tau$ is the pseudo time step, R is the net flux evaluated on a grid point using the fifth-order WENO scheme.

4.4.2 Gauss-Seidel Line Relaxation [4]

To enhance diagonal dominance, a first order scheme is used for the implicit pseudo temporal terms. Following the procedure in Hu's Ph.D. thesis [4], the implicit discretized form of Eq. (4.2) is written as the following

$$\begin{aligned}&\bar{B}\Delta Q^{n+1}_{i,j,k} + A^{+}\Delta Q^{n+1}_{i+1,j,k} + A^{-}\Delta Q^{n+1}_{i-1,j,k} + B^{+}\Delta Q^{n+1}_{i,j+1,k} \\ &+B^{-}\Delta Q^{n+1}_{i,j-1,k} + C^{+}\Delta Q^{n+1}_{i,j,k+1} + C^{-}\Delta Q^{n+1}_{i,j,k-1} = \mathbf{RHS}^{n}\end{aligned} \tag{4.19}$$

$\mathbf{RHS}^{n}$ is the summation of all the terms on the right hand side (RHS) of the equation.

$$\begin{aligned}\mathbf{RHS}^{n} = \Delta t \Big\{ &\Big[\Big(\mathbf{R}^{n}_{i+\frac{1}{2}} - \mathbf{R}^{n}_{i-\frac{1}{2}}\Big) + \Big(\mathbf{S}^{n}_{j+\frac{1}{2}} - \mathbf{S}^{n}_{j-\frac{1}{2}}\Big) + \Big(\mathbf{T}^{n}_{k+\frac{1}{2}} - \mathbf{T}^{n}_{k-\frac{1}{2}}\Big)\Big] \\ &- \Big[\Big(\mathbf{E}^{n}_{i+\frac{1}{2}} - \mathbf{E}^{n}_{i-\frac{1}{2}}\Big) + \Big(\mathbf{F}^{n}_{j+\frac{1}{2}} - \mathbf{F}^{n}_{j-\frac{1}{2}}\Big) + \Big(\mathbf{G}^{n}_{k+\frac{1}{2}} - \mathbf{G}^{n}_{k-\frac{1}{2}}\Big)\Big]\Big\} + D^{n}\cdot\Delta t\end{aligned} \tag{4.20}$$

Gauss-Seidel line relaxation is applied in each direction (i, j, k) and is swept one time step forward and backward in each direction. For example, the equation for Gauss-Seidel relaxation following lines along direction i with the index from small to large is written as:

$$B^{-}\Delta Q^{n+1}_{i,j-1,k} + \bar{B}\Delta Q^{n+1}_{i,j,k} + B^{+}\Delta Q^{n+1}_{i,j+1,k} = \mathbf{RHS}' \tag{4.21}$$

where

$$\mathbf{RHS}' = \mathbf{RHS}^{n} - A^{+}\Delta Q^{n}_{i+1,j,k} - A^{-}\Delta Q^{n+1}_{i-1,j,k} - C^{+}\Delta Q^{n}_{i,j,k+1} - C^{-}\Delta Q^{n+1}_{i,j,k-1} \tag{4.22}$$

4.5 Boundary Conditions

To obtain a well posed solution of a given flow problem by solving the Navier-Stokes governing equation, Eq.(3.11), it is necessary to define the boundary conditions for the problem. Since the solution points are located at the centroids of the cells, ghost cells are used to define the boundaries except for the inviscid flux on wall surface for steady state problems. In other words, most of the boundary conditions are defined by setting up the values of the variables at the ghost cells. Depending on the scheme order of accuracy to be used, the number of ghost cells will vary to match the accuracy of the inner points. Several commonly used boundary conditions are described as the following.

4.5.1 Supersonic Inflow

For supersonic inflow boundary, all the primitive variables are fixed as the initial values of the flow field at the ghost cells.

$$\rho_{gst} = \rho_{int}, u_{gst} = u_{int}, v_{gst} = v_{int}, w_{gst} = w_{int}, e_{gst} = e_{int} \tag{4.23}$$

where, *gst* represents the ghost cell and *int* represents the initial value. In this case, the initial values are set to the values of the free stream and used to specify the inflow BCs.

4.5.2 Wall Boundary

Stationary Walls

For inviscid flux, the wall boundary condition is enforced by setting the normal contravariant velocity on the boundary to zero. For example, if a wall boundary is on a η-surface, the contravariant velocity V is zero on the wall surface, and hence the flux on the wall surface is calculated as,

$$\mathbf{F_w} = \begin{bmatrix} \rho V \\ \rho uV + m_x p \\ \rho vV + m_y p \\ \rho wV + m_z p \\ (\rho e + p)V \end{bmatrix}_w = \begin{bmatrix} 0 \\ m_x p \\ m_y p \\ m_z p \\ 0 \end{bmatrix}_w \tag{4.24}$$

The wall pressure is extrapolated from inner points by the following formulation:

1) 1st order extrapolation

$$p_w = p_1 \tag{4.25}$$

2) 3rd order extrapolation

$$p_w = \frac{1}{6}(11p_1 - 7p_2 - 2p_3) \tag{4.26}$$

For viscous flux, a no-slip and adiabatic wall boundary condition is constructed by setting the ghost cell velocity as the negative of the velocity of its inner counterpart based

on the reflection condition.

$$\rho_{gst} = \rho_{inn}, u_{gst} = -u_{inn}, v_{gst} = -v_{inn}, w_{gst} = -w_{inn}, e_{gst} = e_{inn} \tag{4.27}$$

Chapter 5

Grid Study

The numerical method used in this work utilizes a structured multi-block grid system. This structured grid system consists of hexahedral cells and there are many ways to construct three dimensional multi-block grids for the problem.

All the problems considered and presented in this study have axisymmetry and one of the natural ways to construct a grid taking advantage of this symmetry is to rotate the two dimensional plane about the axis of symmetry. However, this introduces singularity problems to the cells along the axis of symmetry or the stagnation streamline because all those cells then have a wedge-like shape instead of hexahedral shape which makes the area of one of the surfaces zero. Hence, to construct grid systems that are free of singularity, two different grids are constructed based on different topologies. Examples are given below.

5.1 Mixed H-type and O-type Grid

The first type of grid combines O-type grid with H-type grid. The inner block is a cylindrical shaped H-type mesh while the outer block is O-type mesh surrounding the inner block. The left panel of Fig. [5.1] shows the 3D grid used for a hemispherical blunt body. The outer region is divided into 32 blocks of 64x64x4 x-y-z cells each that go to 32 processors. The inner region at the tip of the body, shown magnified in the right panel, is divided into 4 blocks of 64x16x16 cells each that go to 4 processors. Figs. [5.2] and Fig. [5.3] compare

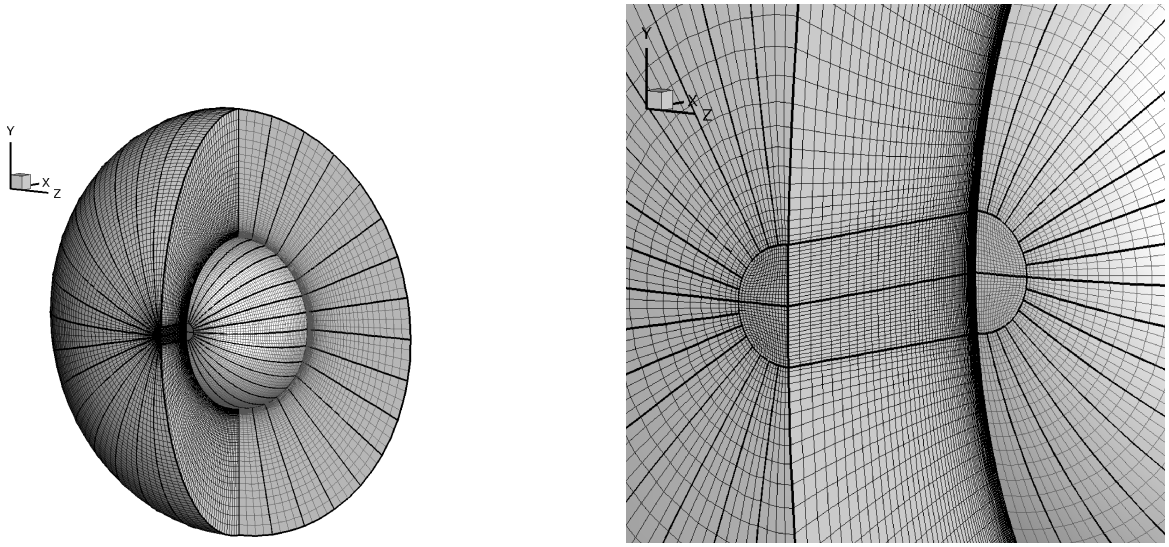

Figure 5.1: Views of the grid for the symmetric blunt body.

the chemically frozen air pressure and temperature along the stagnation streamline, and along a radial line at 45° from the flow direction for different grid densities. The results agree very well, and we have settled on the grid of Fig. [5.1] for the the presentation of our other results.

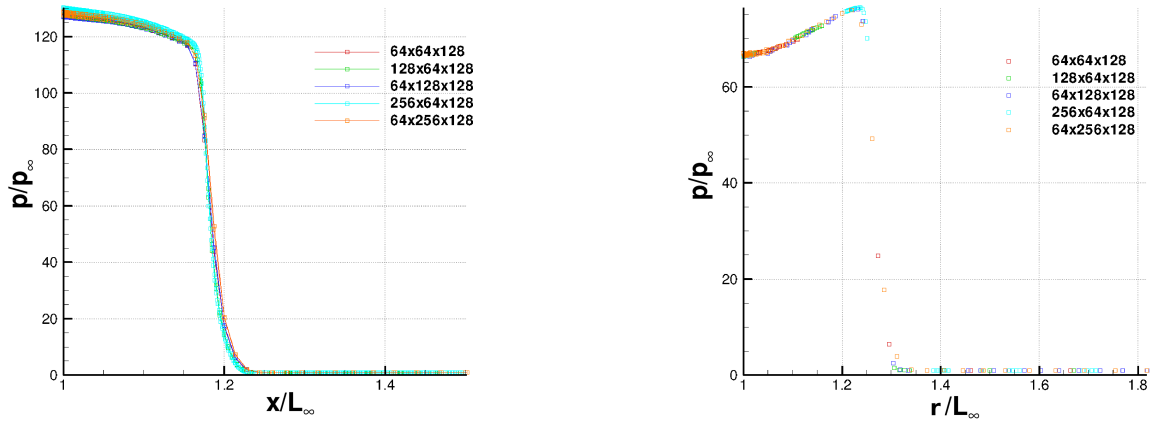

Figure 5.2: Frozen air pressure profiles for different grid densities. The left panel along the stagnation streamline and the right panel along a radial line at 45° from the flow direction.

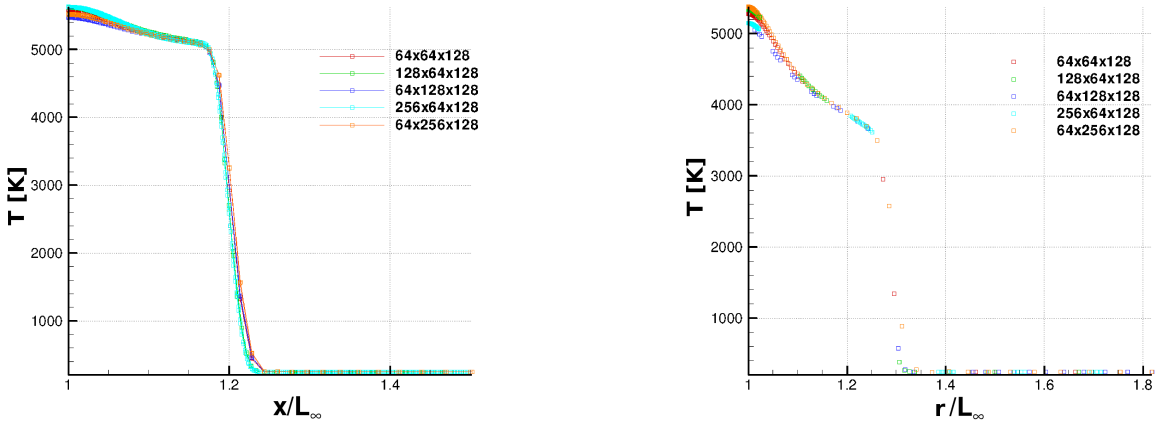

Figure 5.3: Frozen air temperature profiles for different grid densities. The left panel along the stagnation streamline and the right panel along a radial line at 45° from the flow direction.

5.2 Projected H-type Grid

The second type of grid is contructed by projection of a 2 dimensional H-type mesh onto the axisymmetric body geometry to eliminate the singularity along the axis of symmetry

and collateral alignment of two adjacent surfaces both of which cause a numerical difficulty. An example of such a grid system is shown in the following. Fig. [5.4] shows a computational grid comprised of 12 blocks, each of which has 64x8x8 cells. To find out

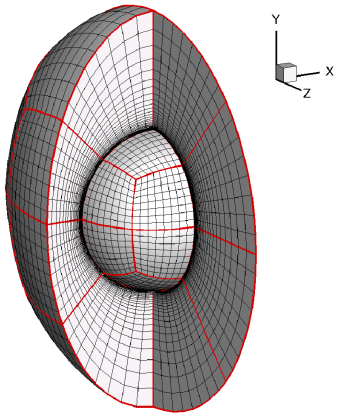

Figure 5.4: Computational grid.

a suitable cell density for the simulations, three computational grids of 12 blocks with different cell densities, i.e., 64x8x8, 96x12x12, and 128x16x16 are compared. Note that the total number of cells in each grid are 64x8x8x12, 96x12x12x12, and 128x16x16x12, respectively. The grids are used to compute Mach 3 equilibrium flow at an altitude of 40km around a hemisphere with isothermal wall of $T_W = T_\infty$. The freestream conditions are u_∞=951.6m/s, p_∞=287.1Pa, T_∞=250.35K, and $\rho_\infty = 3.996 \times 10^{-3}\mathrm{kg/m^3}$. The Reynolds number is 2375 with a characteristic length L_∞=0.01m and the flow is treated as laminar. The pressure and temperature distributions computed with [64x8x8]x12 and [128x16x16]x12 cells are compared in Fig. [5.5]. Both grids result in very similar flow structures and predict an almost identical shock locations. Although the grid with higher

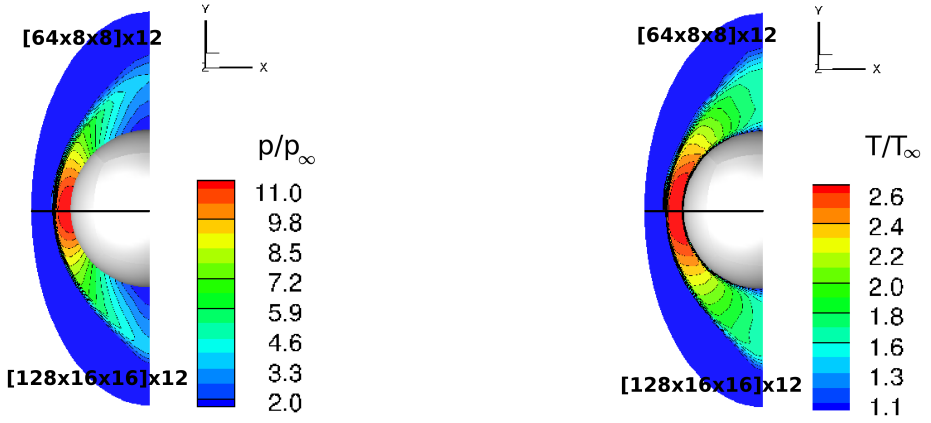

Figure 5.5: Comparison of pressure and temperature distributions for different cell densities.

cell density resolves the shock a little better, the difference is minute. This can be seen more clearly in Fig. [5.6]. The magnetic effects depend on the magnetic interaction param-

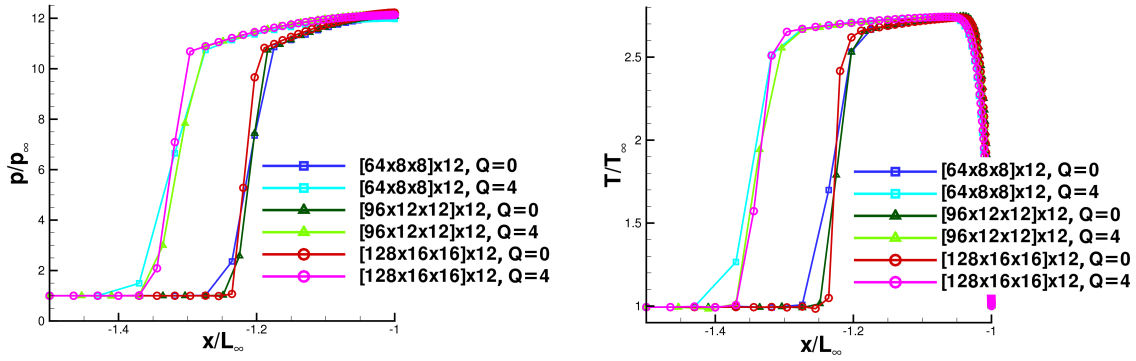

Figure 5.6: Comparison of pressure and temperature profiles for different cell densities.

eter Q, where $Q = \frac{\sigma_{e,ref} B_{ref}^2 L_\infty}{\rho_\infty U_\infty}$. The pressure and temperature profiles along the stagnation streamline are plotted for the non-magnetic case, as well as the magnetic case with Q=4, based on three different grids. All three grids result in almost identical shock locations

along the stagnation streamline with less than a 2% difference with respect to the shock stand-off distance. Thus, considering the large number of simulations to be carried out in this study, the computational grid consisting of 12 blocks of 64x8x8 cells is used, which clearly reveals the effects of the magnetic field on the flow structure.

Chapter 6

Validation

The simulations are validated by comparing the results for Mach 5 laminar flow around a 3D hemisphere at an altitude of 40km with those in the paper by Damevin and Hoffmann [19]. The parameters are u_∞=1586m/s, p_∞=287.1Pa, T_∞=250.35K, and L_∞=0.01m.

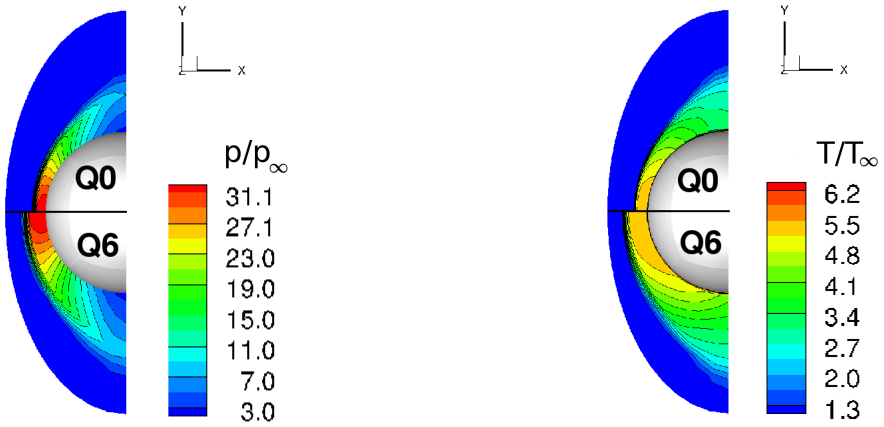

Figure 6.1: Comparison of pressure and temperature distribution for Q=0 and Q=6.

The results for equilibrium air are compared because in this speed regime the use of ideal air tends to exaggerate the temperature. The magnetic effects depend on the magnetic in-

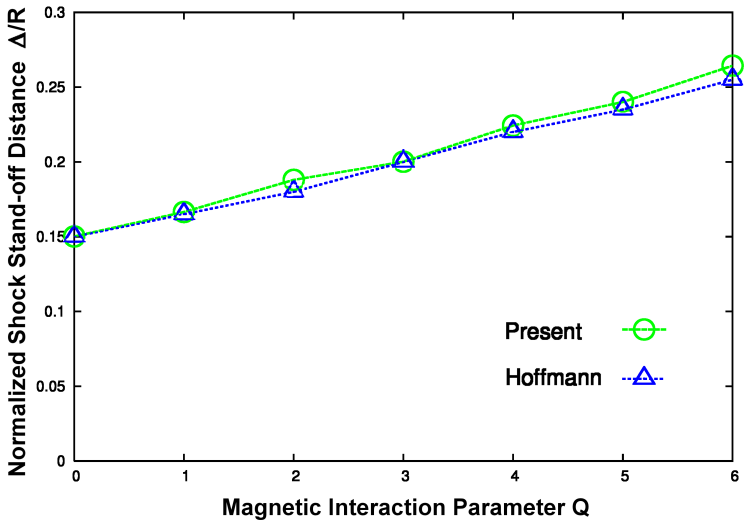

Figure 6.2: Shock stand-off distance vs. interaction parameter.

teraction parameter Q. It is important to note from the definition of $Q = \frac{\sigma_{e,ref} B_{ref}^2 L_\infty}{\rho_\infty U_\infty}$, that the same Q is achieved with smaller B_{ref} when L_∞ is large. Fig. [6.1] shows the comparison of the pressure and the temperature distributions for interaction parameters Q=0 and Q=6. In this case Q=6 corresponds to B_{ref}=2.706T. This large B_{ref} is the consequence of very small L_∞. Here it can be seen that the applied magnetic field moves the shockfront away from the body increasing the shock stand-off distance, and the highest pressure and temperature regions in the vicinity of the nose of the body are significantly enlarged. Also, due to the high temperature gas effect, the stagnation temperature is lower than that of a perfect gas which would be about 6.0. Fig. [6.2] shows the results obtained in this study for various applied magnetic field strengths, with magnetic interaction parameters from Q=1 to Q=6, show good agreement with Hoffmann's result in [21].

Chapter 7

Mach 6 Equilibrium Flow at an Altitude of 40km

Now we consider Mach 6 equilibrium air flow at an altitude of 40km around a 3D hemisphere. The grid described in 5.1 is used for this computation. At this time, we use the actual flow condition for 40km, and the Reynolds number is 4750 with L_∞=0.01m. The wall is assumed to be isothermal with the wall temperature T_W=1250K, and the magnetic field strength is set to correspond to Q=4. We survey two ionization models, an equilibrium ionization model and a power-law-onset ionization model. The so called equilibrium ionization model assumes the electrical conductivity of the air is a constant $\sigma_{e,equil}$=100S/m throughout the entire shock layer, but, considering the temperature variation in the shock layer of the flow this assumption can hardly be justified. So, we introduce electrical conductivity $\sigma_{e,1500K}$=100S/m above 1500K, and $\sigma_{e,1500K}$=0 below 1500K. But, we will still call it an equilibrium model. We introduce a variable electrical conductivity model based on a power-law. We assume the electrical conductivity of the partially ionized air is approximated by $\sigma_e = \sigma_{e,1500K}(\frac{T}{T_0})^k$, where $\sigma_{e,1500K}$=100S/m, T_0 is the stagnation temperature, and k is the exponent of the power-law-onset model. In this study we present

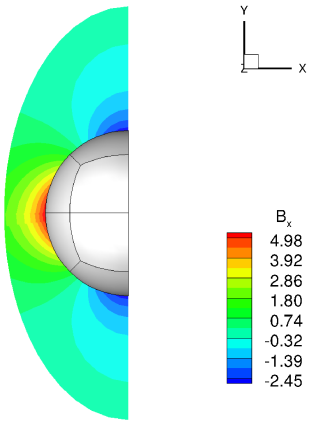

Figure 7.1: Distribution of the x component of the applied magnetic field.

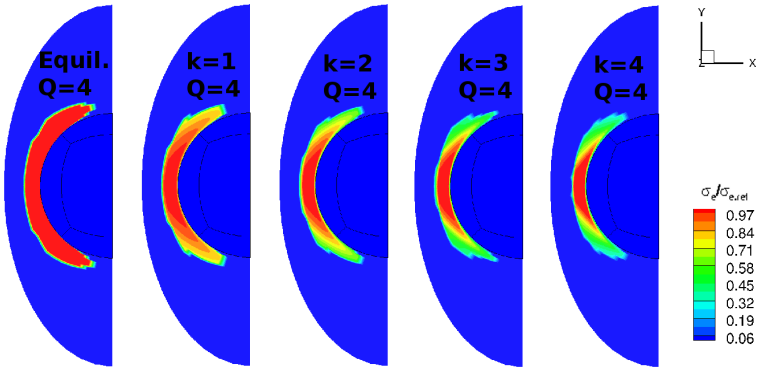

Figure 7.2: Distribution of the electrical conductivity for the equilibrium and the power-law-onset model with various exponents.

the results with several k, where k=0 corresponds to an electrical conductivity that is constant above the onset temperature. Fig.[7.1] shows the applied magnetic field around the hemisphere. The magnetic dipole is located at the center of the hemisphere with its axis aligned with x axis, and the reference point for its strength is at the stagnation point of the body. Fig.[7.2] shows the distribution of the nondimensional electrical conductivities

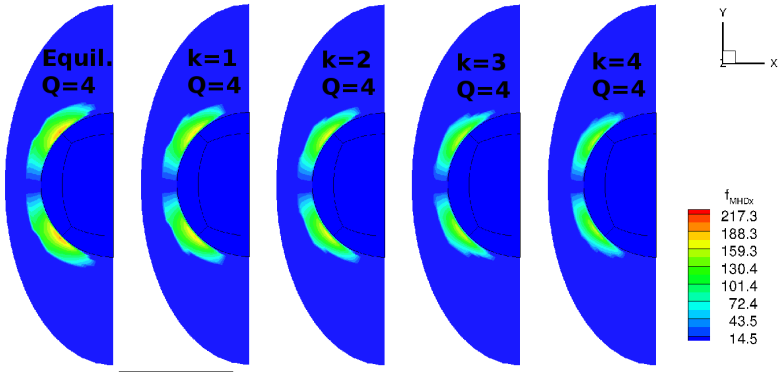

Figure 7.3: Distribution of the MHD force density for the equilibrium and the power-law-onset model with various exponents.

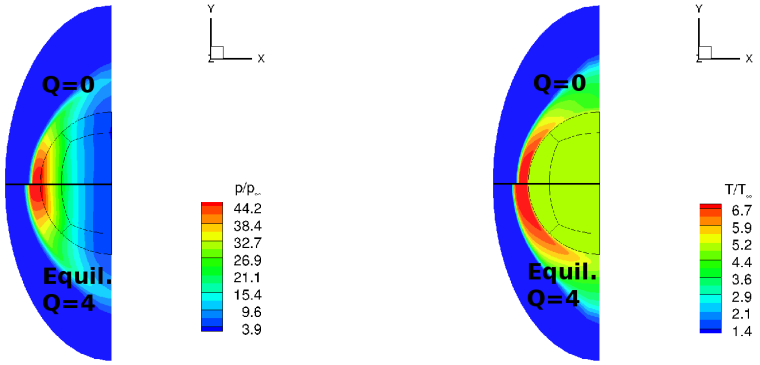

Figure 7.4: Comparison of pressure and temperature field for Q=0 and Q=4 for equilibrium model.

for the equilibrium ionization model and power-law-onset model with different exponents from k=1 to 4. It can be seen that the electrical conductivity for the equilibrium model is constant throughout the high temperature region. It is clear that where the temperature is lower the conductivity diminishes. The conductivity in the outer portions of the flow diminishes as k increases as expected. Also, the MHD force density distributions for each models are shown in Fig.[7.3]. Fig.[7.4] compares the pressure and the temperature dis-

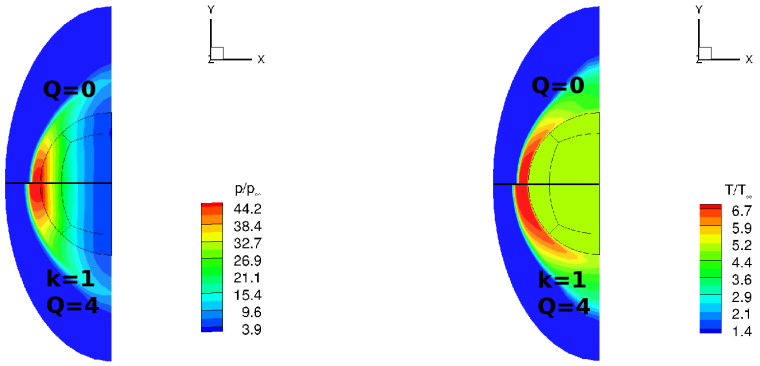

Figure 7.5: Comparison of pressure and temperature fields for Q=0 and Q=4 for power-law-onset model.

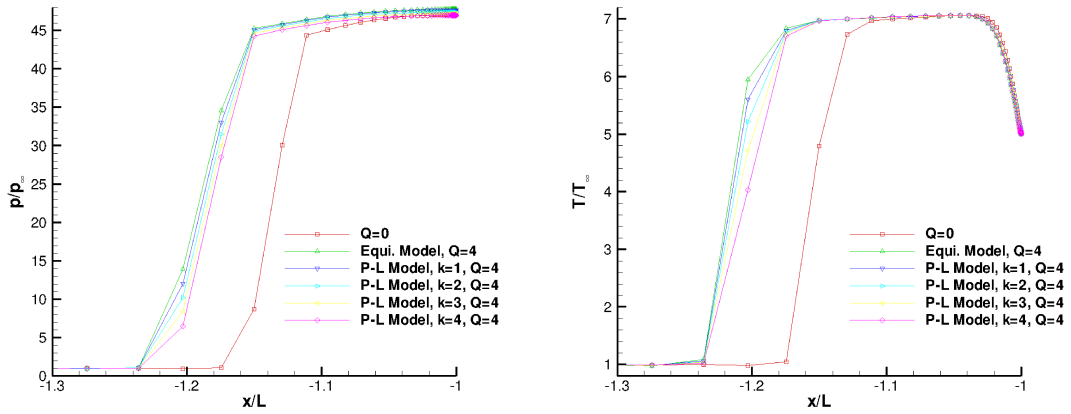

Figure 7.6: Pressure and temperature profiles of equilibrium model and power-law-onset model with various exponents.

tributions for Q=0 and Q=4 for the equilibrium model. Here, we can see the same effects observed in the validation case. Fig.[7.5] shows the pressure and temperature distributions for Q=0 and Q=4 for the exponent k=1. The overall changes in the flow fields are the same as the equilibrium model. Now, Fig.[7.6] compares two ionization models with various k values. Here, we can see that the power-law-onset model predicts a smaller effect in shock

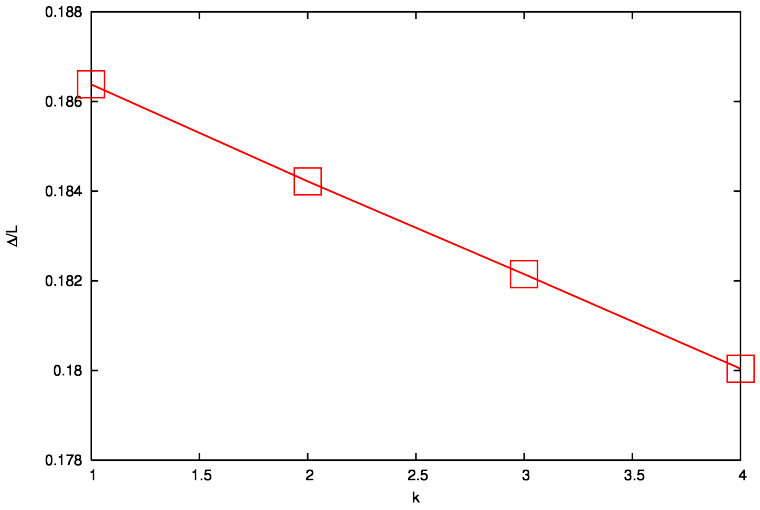

Figure 7.7: Shock stand-off distance vs. exponent k of the power-law-onset.

standoff distance change but with the same stagnation pressure and temperature. Also, as the exponent becomes larger the change in the shock stand-off distance becomes smaller, and there is a linear proportionality between the change in the shock stand-off distance and the exponent k as shown in Fig.[7.7]. Note that there is no net force in the vicinity of the stagnation point of the body.

Chapter 8

Mach 6 Equilibrium Flow at an Altitude of 70km

Fig.[8.1] shows the basic flow fields of Mach 6 equilibrium flow at an altitude of 70km around a hemisphere of radius R=1.0m. The wall is assumed to be isothermal with the

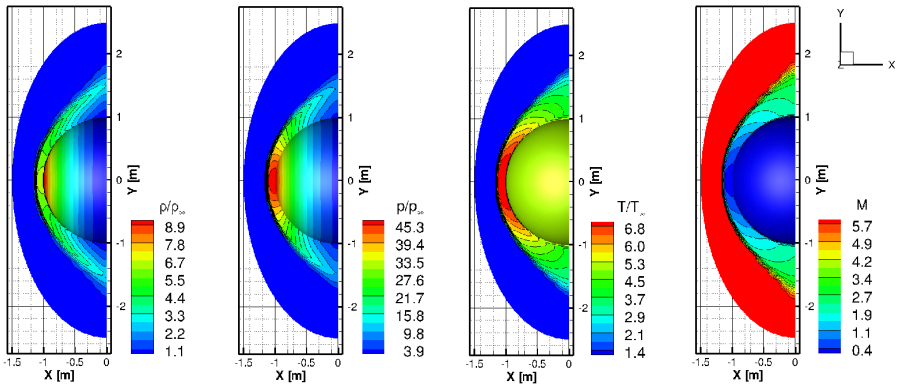

Figure 8.1: Basic flow fields of a Mach 6 equilibrium flow at an altitude of 70km.

wall temperature T_W=1098K.

The magnetic interaction parameter is proportional to the characteristic size of the body, and the magnetic field to achieve the same magnetic interaction parameter is in-

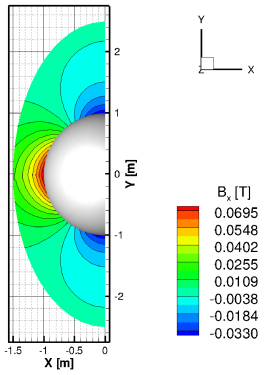

Figure 8.2: X component of the external magnetic field of dipole.

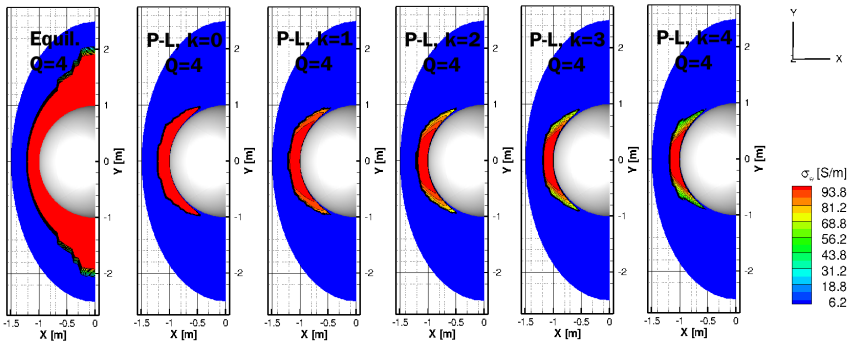

Figure 8.3: Electrical conductivity distribution for equilibrium ionization model and power-law-onset model.

versely proportional to the square root of the characteristic length of the body. Thus, instead of considering a small body size which requires a very strong magnetic field strength for a given magnetic interaction, we now consider a meter scale body so that the magnetic field strength required is more realistic. A magnetic dipole is located at the center of the hemisphere with its axis aligned with the x axis as before, and its x component is shown Fig.[8.2]. Here, with L_∞=1.00m Q=4 is achieved with the magnetic field of 0.0768T. Fig.[8.3] compares the electrical conductivity distributions based on the equilib-

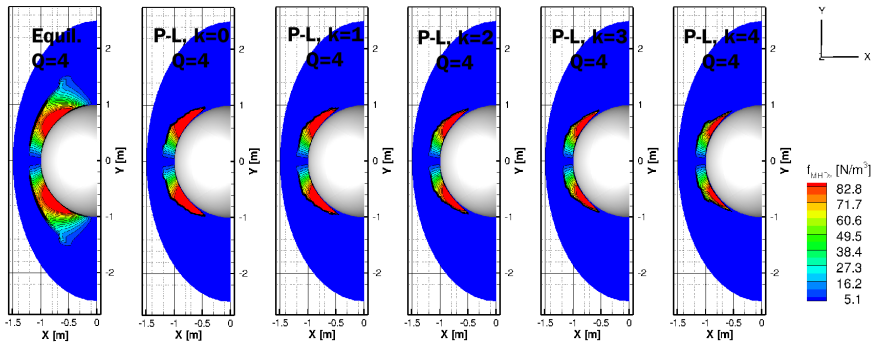

Figure 8.4: MHD force density distributions for equilibrium ionization model and power-law-onset model.

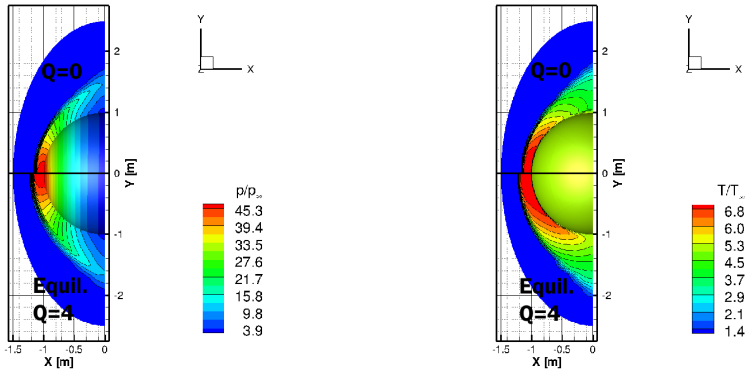

Figure 8.5: Comparison of pressure and temperature distribution for equilibrium model for Q=0 and 4.

rium and power-law-onset ionization models with different exponent from k=0 to 4. Here, we assumed the original equilibrium ionization model so that the entire shock layer has a constant electrical conductivity $\sigma_e = \sigma_{e,equil} = 100$ S/m. The corresponding MHD force density distributions are shown in Fig.[8.4]. The effects of applied magnetic field can be seen in the pressure and the temperature distribution Fig.[8.5] and Fig.[8.6] as well as the pressure and the temperature profiles along the stagnation streamline shown in Fig.[8.7].

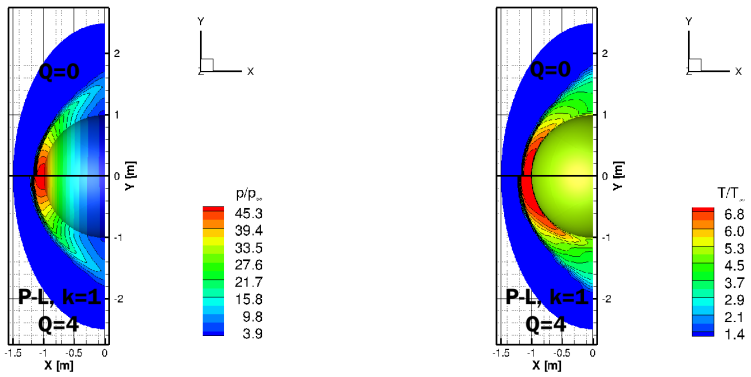

Figure 8.6: Comparison of pressure and temperature distribution for power-law-onset model with k=1 for Q=0 and 4.

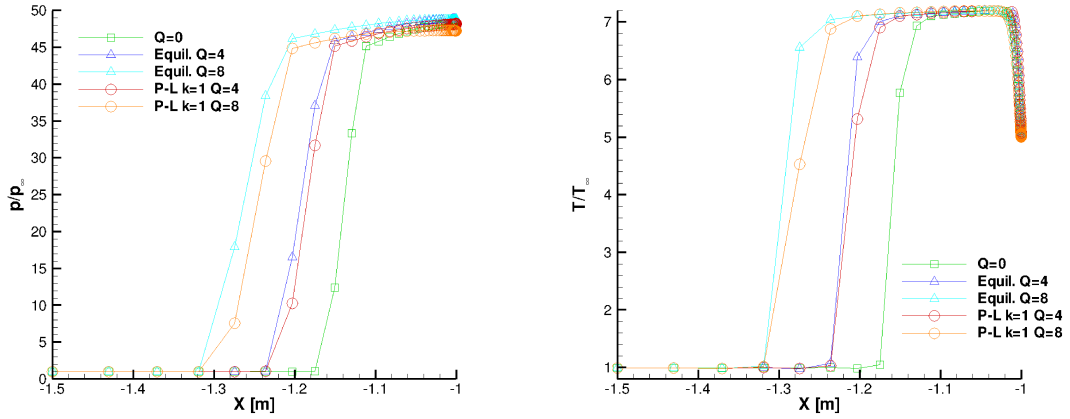

Figure 8.7: Pressure and temperature profiles of equilibrium model and power-law-onset model with k=1 for Q=0, 4, and 8.

A much larger region is occupied by the constant electrical conductivity of the equilibrium model compared to those of power-law-onset model with various k's, and a different angular variation of the MHD force density distribution is observed for the equilibrium model, especially along the off-center, diagonal direction. Fig.[8.8] compares the effect of the applied magnetic field on the shock stand-off distance for the equilibrium model and

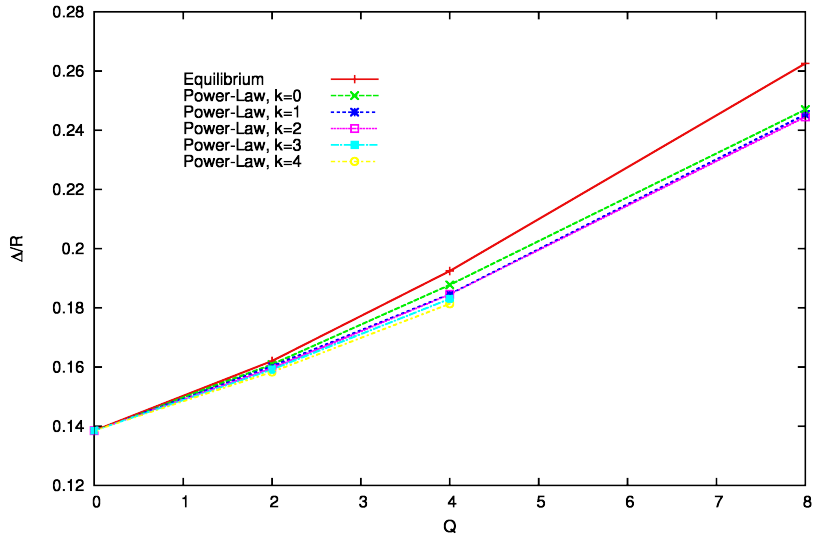

Figure 8.8: Effect of applied magnetic field on the shock stand-off distance based on different ionization models.

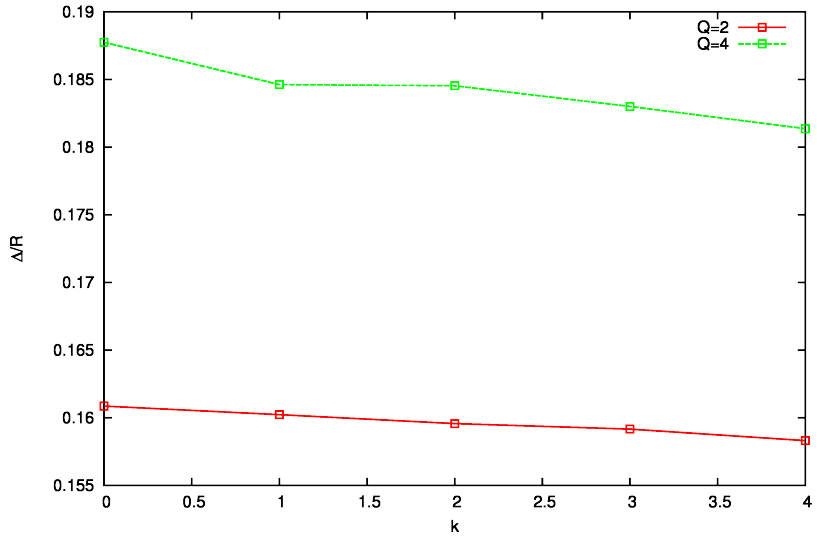

Figure 8.9: Shock stand-off distance vs. exponent k for Q=2 and 4.

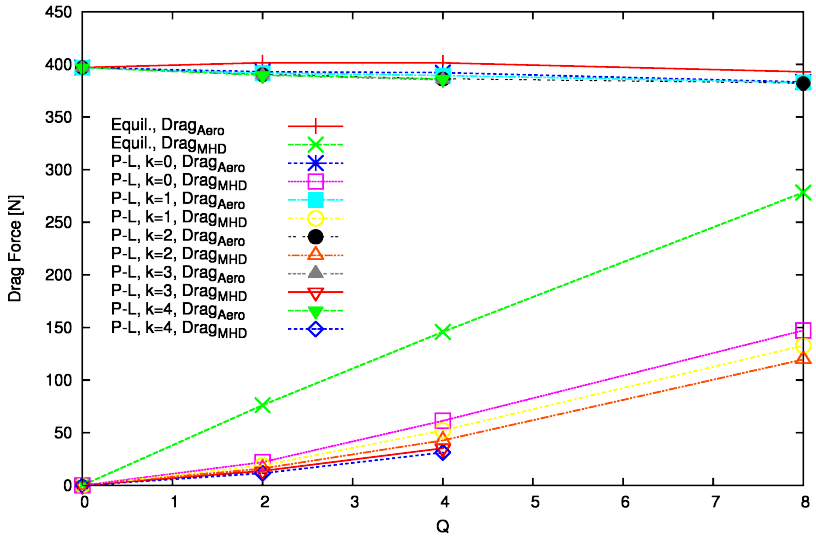

Figure 8.10: Comparison of aerodynamic drag with MHD drag for equilibrium and power-law-onset model with k=0 through 4 for Q=0 through 8

the power-law-onset model with various exponents. The shock stand-off distances based on the different exponents of the power-law-onset ionization model for Q=2 and Q=4 are given in Fig.[8.9]. The MHD drag forces are compared with the aerodynamic drag forces for the equilibrium model and the power-law-onset model with k=0 to 4 in Fig.[8.10]. The aerodynamic drag force for all the cases is concentrated on the top around 400N. This is not surprising because the aerodynamic force is not supposed to be greatly changed by the MHD force. It is clear that the MHD drag force diminishes as k increases. Lastly, the ratio of the MHD drag force to the aerodynamic drag force is compared in Fig.[8.11]. The MHD drag force based on the equilibrium ionization model is predicted to increase to about 70 percent of the aerodynamic drag force with Q=8. Also, there is a good linear proportionality between the ratio of the MHD drag force to the aerodynamic drag force

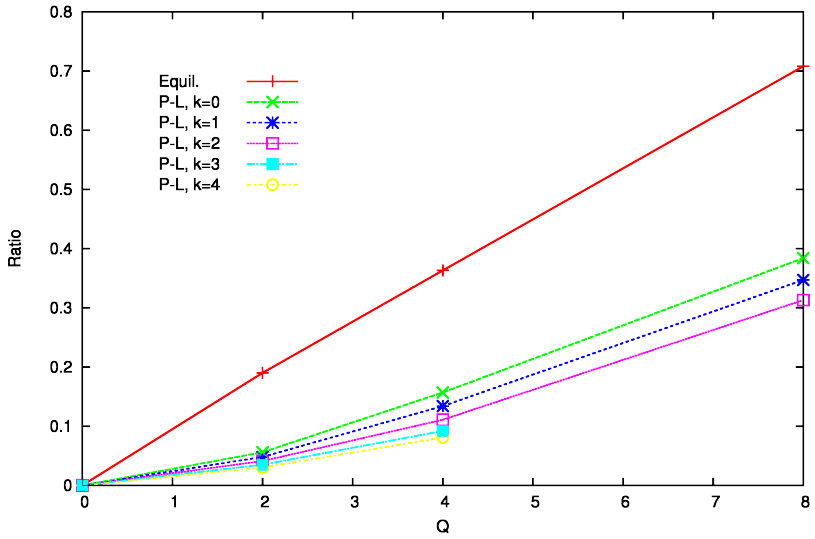

Figure 8.11: Comparison of ratio of MHD drag to aerodynamic drag for equilibrium and power-law-onset model with k=0 through 4 for Q=0 through 8

and the interaction parameter Q. On the other hand, the power-law-onset model predicts considerably smaller ratio between the MHD drag and the aerodynamic drag for all k compared to the equilibrium model, and the slope seems to grow slightly with increasing Q narrowing the relative difference between the two models.

Chapter 9

Mach 15 Equilibrium Flow at an Altitude of 40km

In this section a Mach 15 equilibrium air flow at an altitude of 40km around a 3D hemisphere is considered. The second type of grid described in 5.2 is employed for this computation. The actual flow condition of 40km is used. The flow parameters are $\rho_\infty = 3.996 \times 10^{-3}\text{kg/m}^3$, $p_\infty = 287.1\text{Pa}$, $\text{T}_\infty = 250.35\text{K}$, $a_\infty = 317.19\text{m/s}$, and $\mu_\infty = 1.601 \times 10^{-5}\text{Pa}\cdot\text{s}$. The length of the body is set to one meter ($L = 1$ m), so the desired Q is achieved with realistic magnetic filed strengths ($B_{ref} = 0.2706$ T). The Reynolds number is 1.188×10^6 with L_∞=1.00m. The flow is treated as turbulent and the Baldwin-Lomax turbulence model is used throughout the simulations. The wall is assumed to be isothermal with the wall temperature $\text{T}_\text{W} = 5 \times \text{T}_\infty$=1252K, and the magnetic field strength is set to correspond to Q=2, 4, 6, and 8. The multiblock, structured grid shown in Fig. [9.1] is used throughout the computations. The grid consists of 16 blocks each of which has $64 \times 16 \times 16$ cells.

In our Mach 15 simulations the average convergence error is very small, but the maximum error gives trouble in some locations which are very close to the surface of the

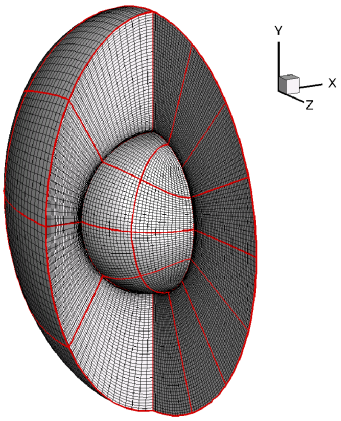

Figure 9.1: Computational grid.

body. Our grid sensitivity work then consisted of estimating the boundary layer thickness and putting smaller computational cells in this layer to reduce the maximum error, while maintaining the same total number of grid cells. The TGAS method is used to simulate

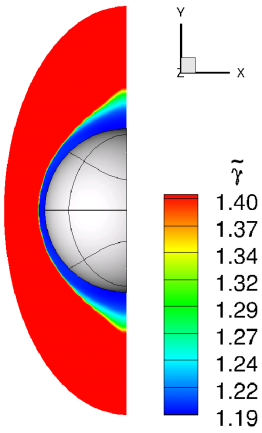

Figure 9.2: Distribution of $\tilde{\gamma}$.

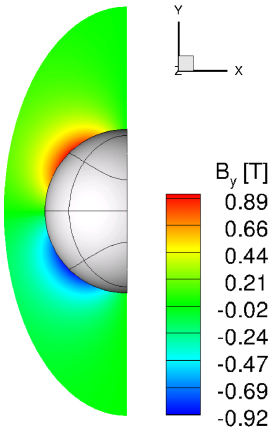

Figure 9.3: Applied magnetic field.

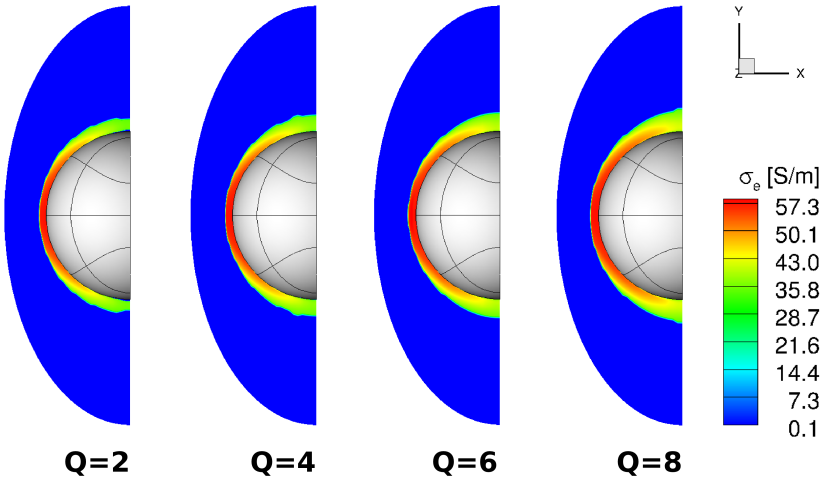

Figure 9.4: Electrical conductivity for P1 with Q=2, 4, 6, and 8 at an altitude of 40km.

the high temperature gas effect and Fig. [9.2] shows the distribution of the ratio of specific heats $\tilde{\gamma}$. It can be seen that the ratio of specific heats is about 1.2 for the most part behind the shock, which is significantly smaller than the value 1.4 it would have been for an ideal gas. A point magnetic dipole is located at the center of the hemisphere with its axis aligned with the x axis, and the reference point for its strength is at the stagnation point of the body. Fig. [9.3] shows B_y of the applied magnetic field around the hemisphere. The magnetic field strength corresponding to Q=8 is 1.233T. Figs. [9.4], [9.5], [9.6], and [9.7] examine the behavior of σ_e and T under several models and conditions. The electrical conductivity of the power-law-onset model with k=1 for Q=2, 4, 6, and 8 is shown in Fig. [9.4]. The region with nonzero electrical conductivity for stronger magnetic interaction is larger than that of weaker magnetic interaction. Note that although the regions with nonzero electrical conductivity differ for various magnetic interaction parameters, their values are mostly similar. Also, the variation of the distribution of electrical conductivity is more

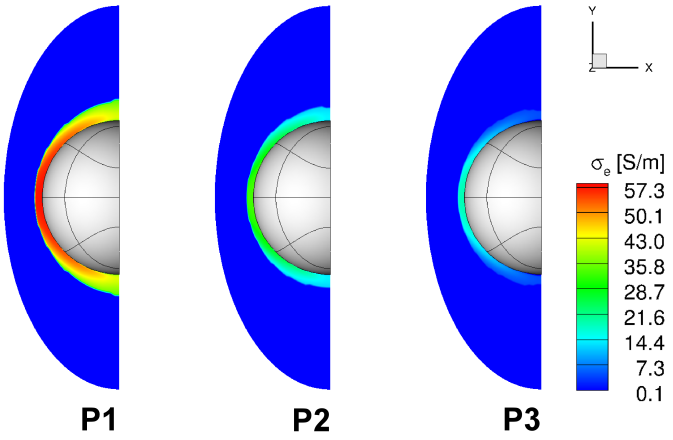

Figure 9.5: Electrical conductivities for different exponents for Q=8.

noticeable around the rear part of the body than the stagnation part. Fig. [9.5] compares the distribution of the electrical conductivities of the power-law-onset model with different exponents k=1, 2, and 3 with magnetic interaction parameter Q=8, and T_{onset}=4,000K. The electrical conductivity diminishes as k increases. Figs. [9.6] and [9.7] compare the pressure and the temperature fields of the power-law-onset model with different powers for Q=8. The strong temperature rise toward the rear of the body is due to the fact that the fluid is being slowed down adiabatically by the magnetic force. There is basically no structural difference in pressure and temperature fields except in the thickness of the shock layer.

The x component of the MHD force density distribution, f_{MHDx}, of the power-law-onset models with different powers for Q=2, 4, 6, and 8 are compared in Fig. [9.8] and Fig.[9.9]. Note that there is no net force in the vicinity of the stagnation point of the body as well as the rearmost part of the body because in those regions the magnetic field and the current are antiparallel. The highest MHD force density occurs around the middle part

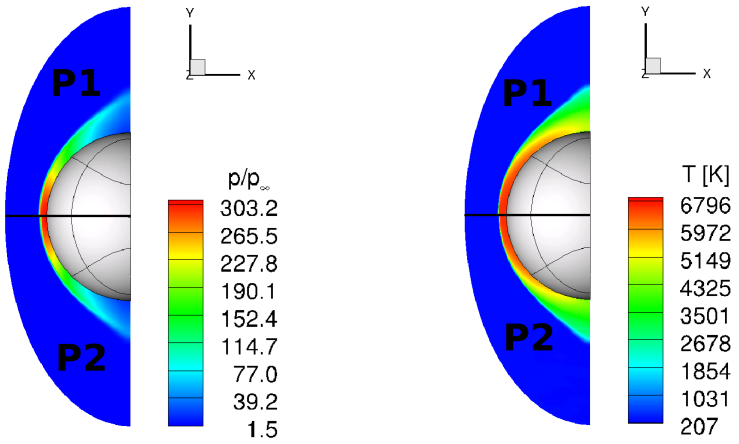

Figure 9.6: Pressure and temperature fields of power-law-onset model with k=1 and k=2 for Q=8.

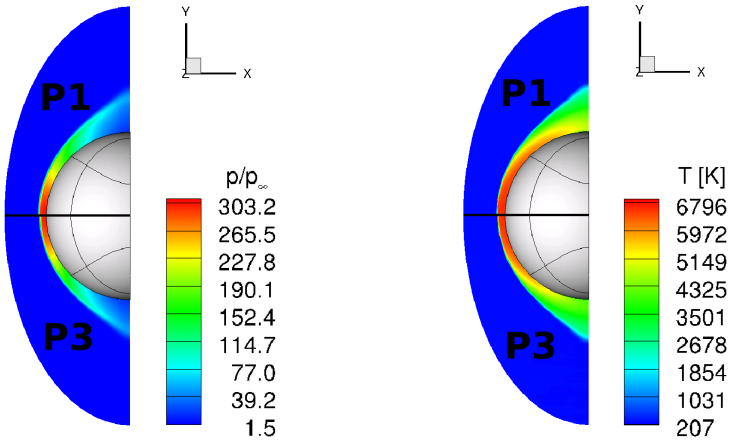

Figure 9.7: Pressure and temperature fields of power-law-onset model with k=1 and k=3 for Q=8.

of the body. The changes in shock stand-off distance for the power-law-onset model with different powers are compared in Fig. [9.10]. It is clear that the shock stand-off distance

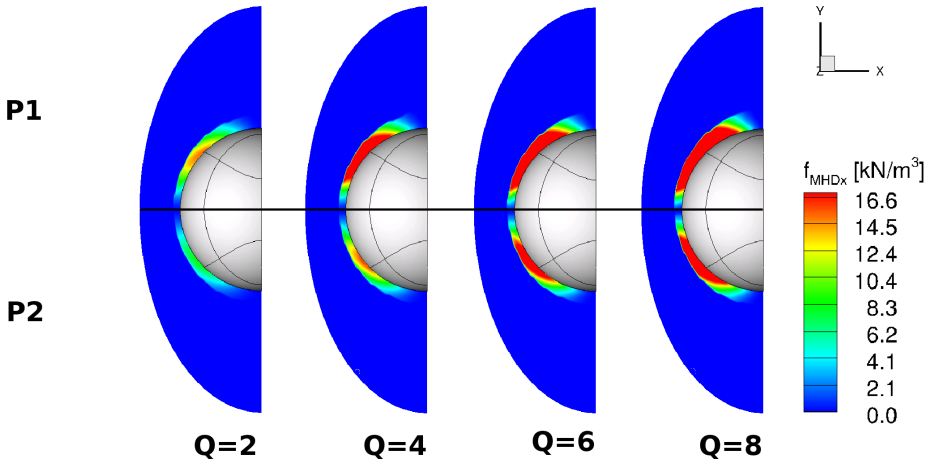

Figure 9.8: MHD force density for k=1 and k=2 with Q=2, 4, 6, 8.

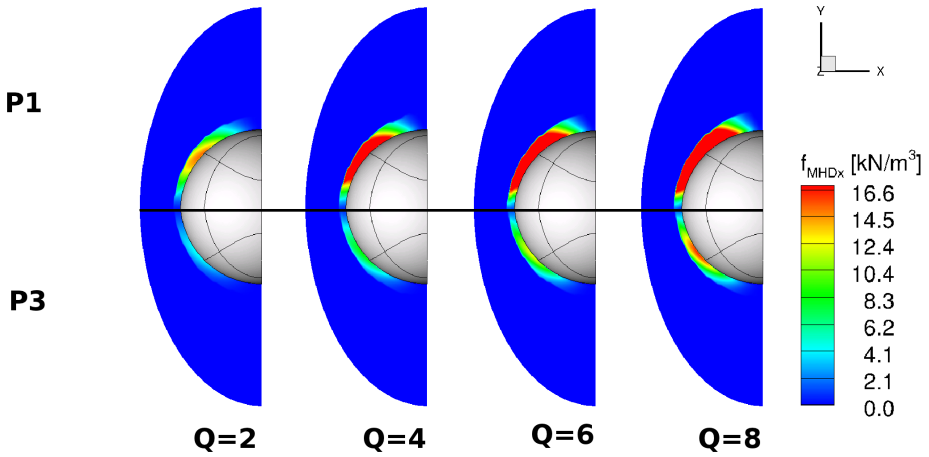

Figure 9.9: MHD force density for k=1 and k=3 with Q=2, 4, 6, 8.

is proportional to the magnetic interaction parameter when k=1, but when k=2 and k=3 the slope is less as Q increases above a certain value. This might be due to the grid in the neighborhood of the shock as mentioned in Section IX. Also, the overall change in shock stand-off distance is much smaller for k=2 and 3 compared to k=1 due to the magnitude of

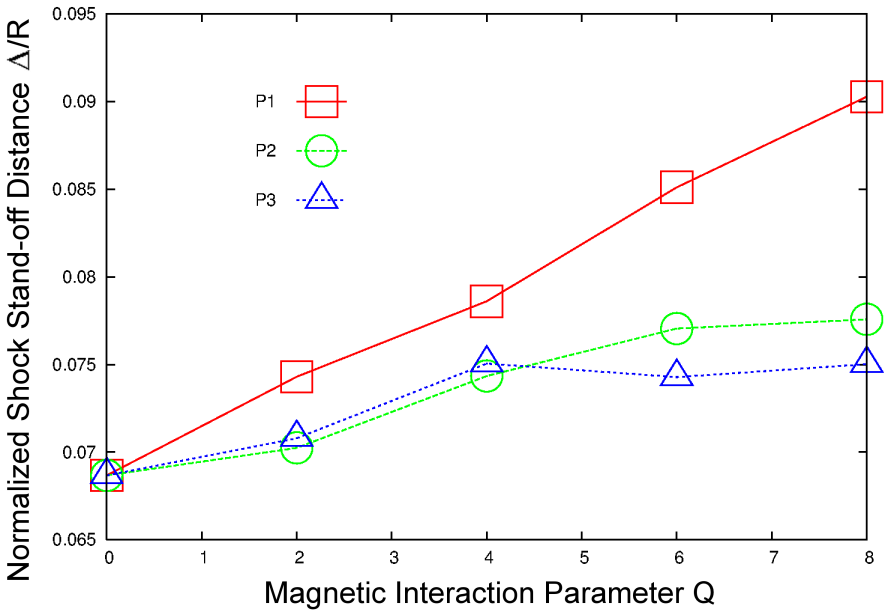

Figure 9.10: Changes in shock stand-off distance of power-law-onset model with different exponents.

the electrical conductivity. Fig.[9.11] shows the ratios of MHD drag force to aerodynamic drag force predicted for different powers for Q=2, 4, 6, and 8. It can be seen that the ratio is proportional to the interaction parameter for all three powers. The MHD drag force becomes 14% of the aerodynamic drag force when Q=8 for k=1 while it is reduced to much less than 10% for k=2 and 3. Therefore, the effect of applied magnetic field on the shock stand-off distance and the MHD drag force is very sensitive to the power of the power-law-onset model. If the power is greater than or equal to 2, the overall effect is expected to be very weak.

For all the previous calculations the onset temperature of the power-law-model has been set to 4,000K. At this temperature O_2 is totally dissociated and N_2 begins to be dis-

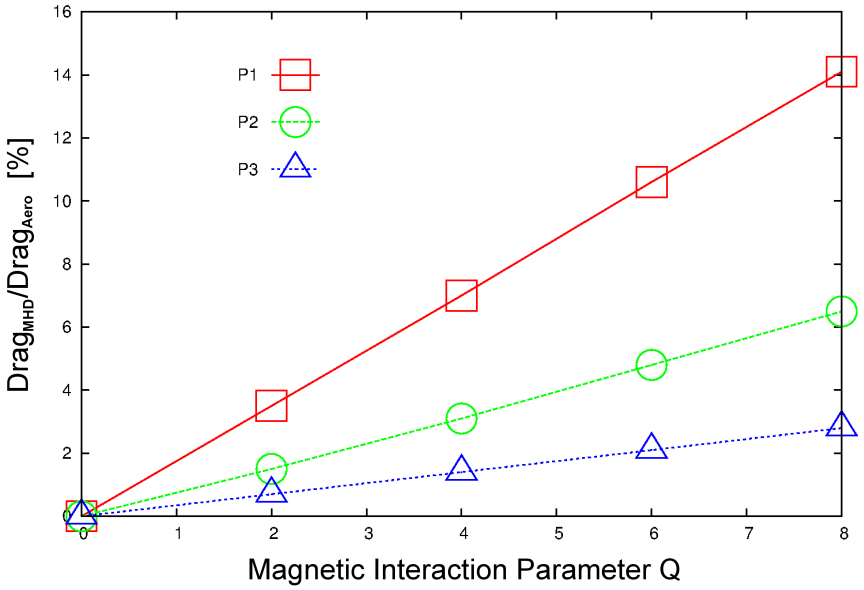

Figure 9.11: Changes in the ratio of MHD drag to aerodynamic drag of power-law-onset model with different exponents.

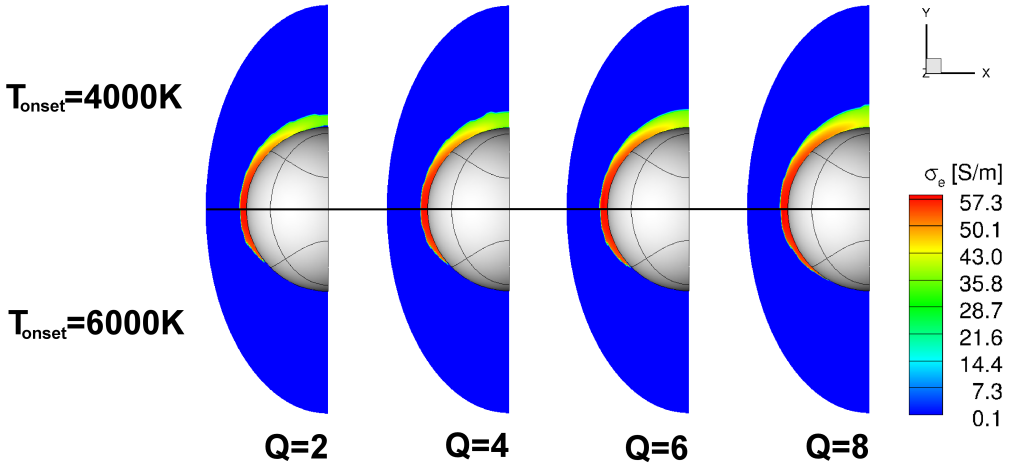

Figure 9.12: Electrical conductivity of power-law-onset model with different onset temperatures for Q=8.

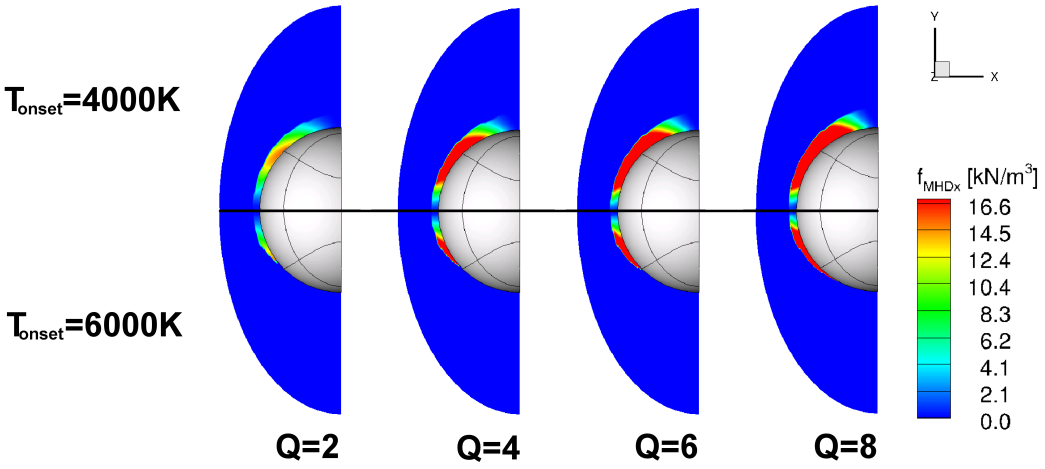

Figure 9.13: MHD force densities of power-law-onset model with different onset temperatures.

sociated. Next, the power-law-onset model with the onset temperature of 6,000K is considered. Fig. [9.12] compares the distribution of electrical conductivity of the power-law-onset model with two different onset temperatures, 4,000K and 6,000K. It can be seen that the region of nonzero electrical conductivity is dramatically reduced with T_{onset}=6,000K. Note that the reduction, however, is not noticeable at the stagnation point throughout the Q values. The MHD force density for the power-law-onset model with the two different onset temperature is compared in Fig.[9.13]. There is almost no MHD force past the middle part of the body in case of 6,000K onset temperature. The effect of applied magnetic field on the shock stand-off distance is compared in Fig. [9.14]. Note that in spite of the big differences in the electrical conductivity and in the MHD force density, the effect of the applied magnetic field on the shock stand-off distance is almost linear up to Q=6, but the slope diminishes above that for $T_{onset} = 6,000$K. Fig. [9.15] compares the ratio of MHD drag force to aerodynamic drag force with the two different onset temperatures. In contrast

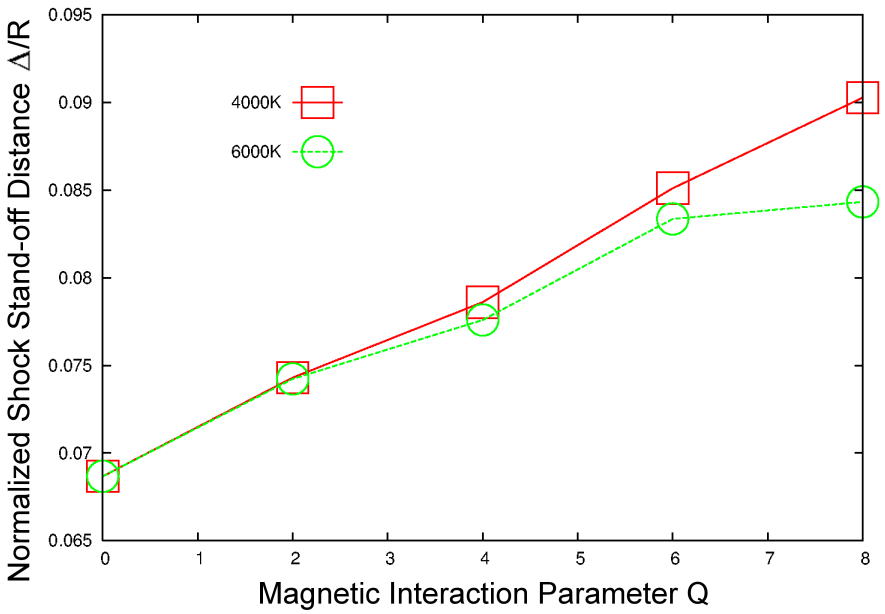

Figure 9.14: Changes in shock stand-off distances of power-law-onset model with different onset temperatures.

to the shock stand-off distance, the ratio of MHD drag force to aerodynamic drag force behaves very differently in the two cases. It seems that the MHD drag force is very small compared to the aerodynamic drag force for T_{onset}=6,000K, and it increases nonlinearly with Q. If it increases like a convex function, then with sufficiently large Q the ratio of MHD drag force to aerodynamic drag force of T_{onset}=6,000K case might be comparable to that of T_{onset}=4,000K case. But, it will still need a very strong magnetic field.

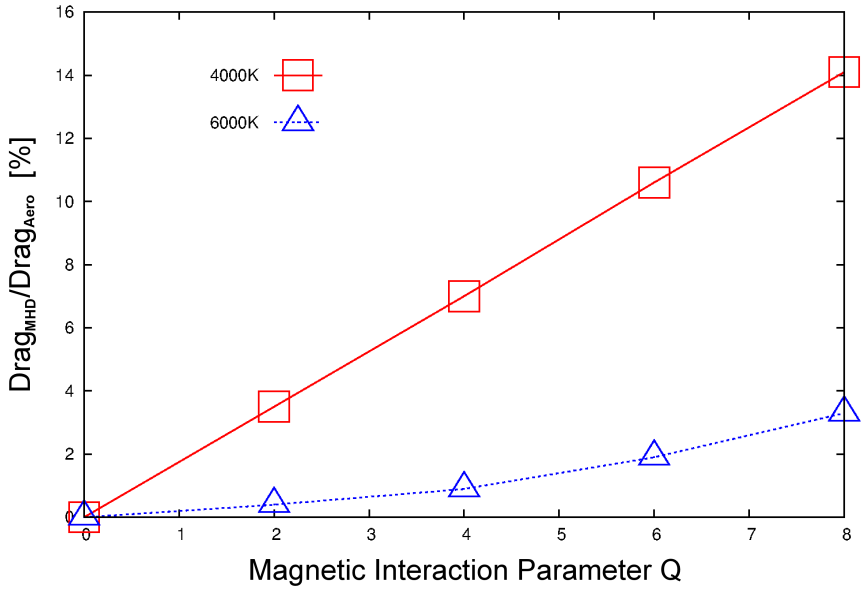

Figure 9.15: Changes in the ratio of MHD drag to aerodynamic drag of power-law-onset model with different onset temperatures.

Chapter 10

Mach 15 Equilibrium Flow at an Altitude of 60km

In this section Mach 15 flow at an altitude of 60km is considered. The parameters are $\rho_\infty = 3.097 \times 10^{-4}\mathrm{kg/m^3}$, $p_\infty = 21.96\mathrm{Pa}$, $\mathrm{T}_\infty = 247.0\mathrm{K}$, $a_\infty = 315.1\mathrm{m/s}$, $\mu_\infty = 1.584 \times 10^{-5}\mathrm{Pa \cdot s}$, and the Reynolds number is 92411. The wall is assumed to be isothermal with the wall temperature $\mathrm{T_W} = 5 \times \mathrm{T}_\infty$=1235K. A magnetic dipole is located at the center of the hemisphere with its axis aligned with x axis as before. Here, with L_∞=1.00m Q=8 is achieved with the magnetic field of 0.342T due to the lower freestream density. The electrical conductivity model used is the power-law-onset model with onset temperature $\mathrm{T_{onset}}$=4,000K and the power k=1. Fig. [10.1] compares the distribution of electrical conductivities at 40km and 60km for various Q. They are comparable to each other except at the rear part of the body where nonzero electrical conductivity region is diminished for 60km compared to 40km. The MHD force density distributions for different altitudes are compared in Fig. [10.2]. In contrast to the electrical conductivity, the MHD force density shows very different features for the two altitudes. It has not just a much diminished region of nonzero MHD force but also much smaller peak values. For example, the peak value

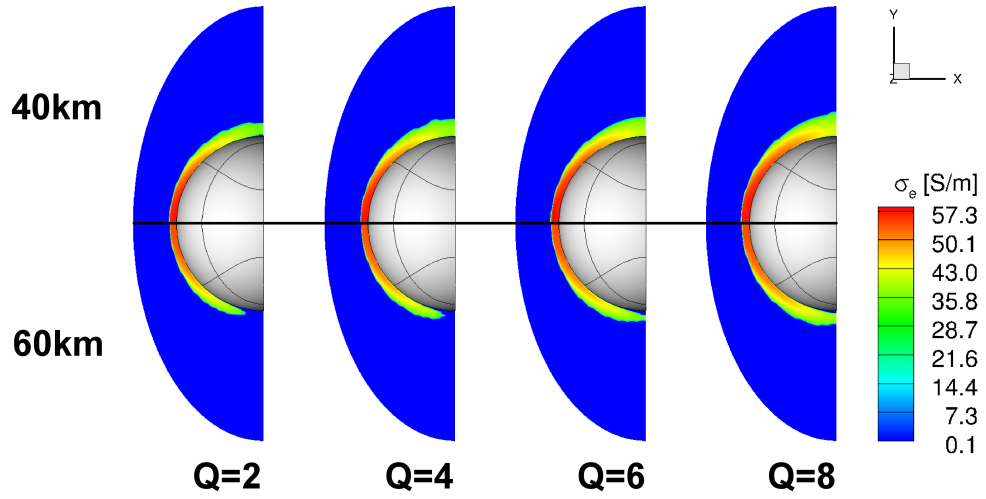

Figure 10.1: Electrical conductivity for Q=2, 4, 6, and 8 at different altitudes.

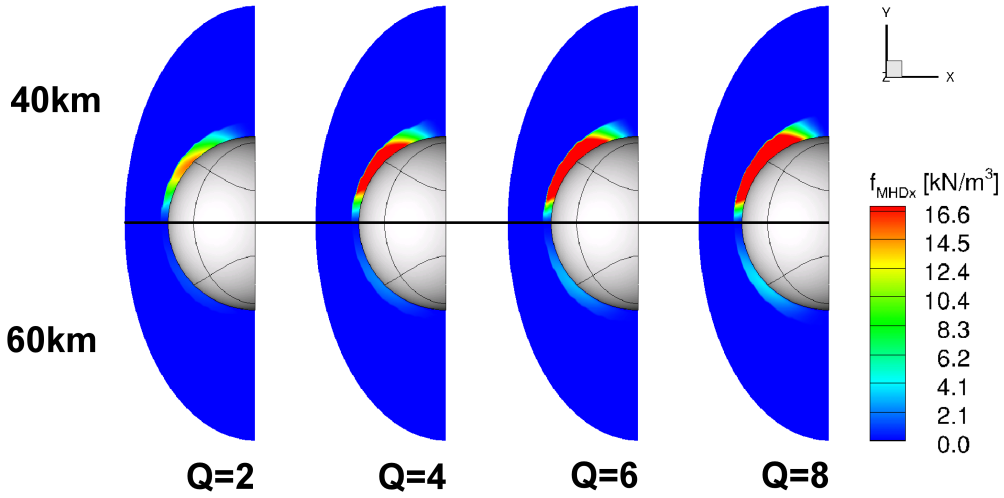

Figure 10.2: MHD force density distributions for Q=2, 4, 6, and 8 at different altitudes.

of the MHD force density for Q=8 is less than a quarter of the 40km counterpart. Fig. [10.3] shows changes in the pressure and the temperature profiles along the stagnation streamline as Q varies at 60km. It shows consistent pressure and temperature throughout

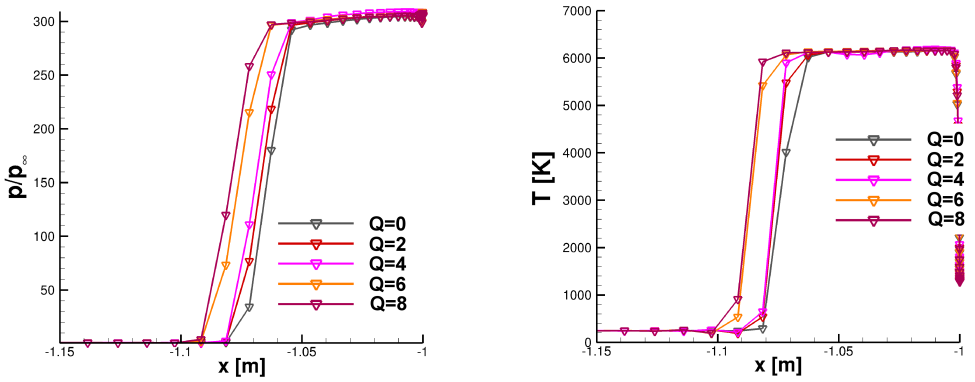

Figure 10.3: Pressure and temperature profiles for Q=0, 2, 4, and 8 with k=1.

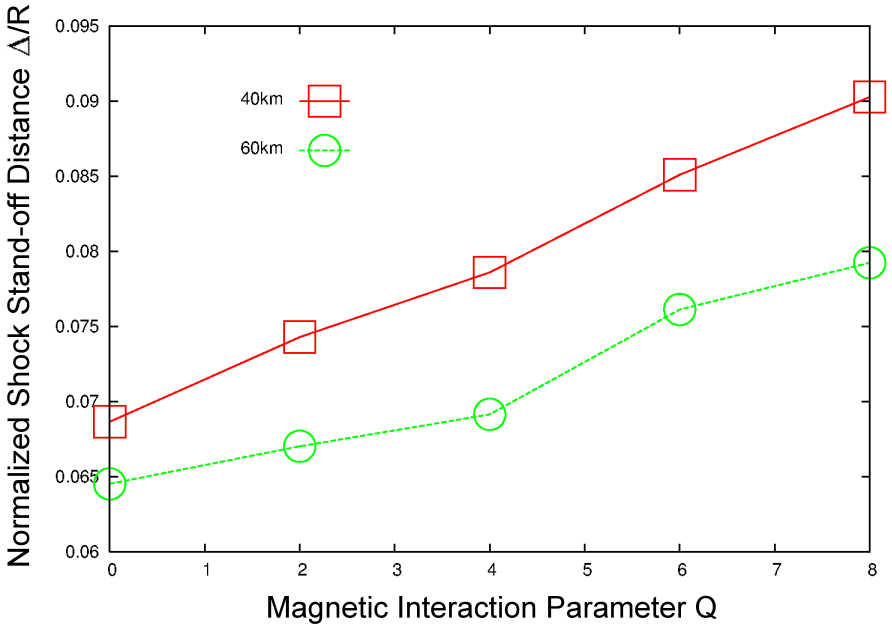

Figure 10.4: Changes in shock stand-off distance at different altitudes.

various Q values even though there is noticeable change in shock stand-off. Fig. [10.4] compares the effect of the applied magnetic field on the shock stand-off distance at two

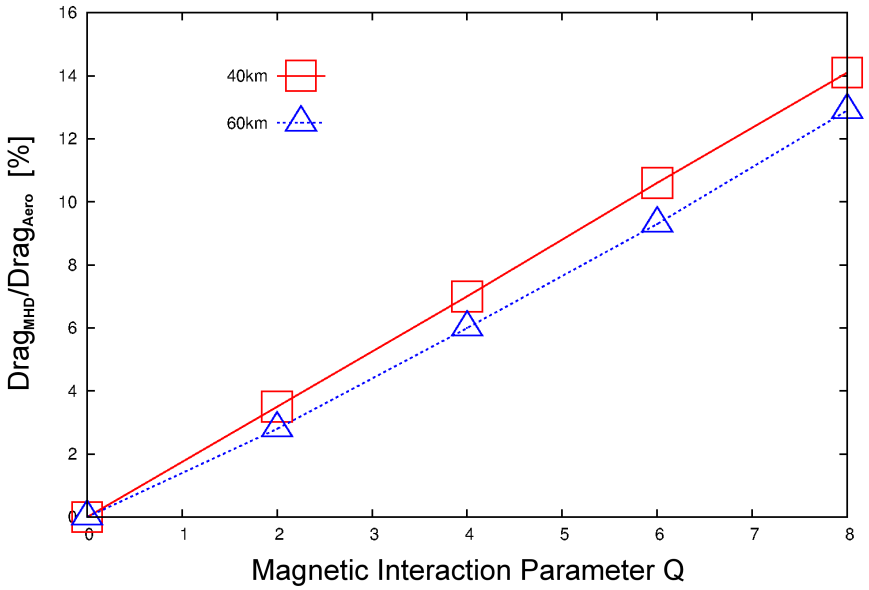

Figure 10.5: Change in the ratio of MHD drag to aerodynamic drag at different altitudes.

different altitudes. The effect for 60km shows similar tendency just with a little smaller proportionality. The ratio of MHD drag force to aerodynamic drag force is compared for the two altitudes in Fig. [10.5]. Again, they behave similarly showing very good linearity and both altitudes show comparable increase in the ratio. Overall, the applied magnetic field has similar effects for the two altitudes for a given magnetic interaction parameter. However, considering the fact that the strength of the applied magnetic field needed to achieve the same magnetic interaction is much weaker for 60km than 40km, it is more efficient to apply the magnetic field at higher altitude.

Chapter 11

Conclusions

This work has demonstrated the successful use of the Low Diffusion Energy Convective Upwind and Split Pressure (ECUSP) scheme with a fifth order Weighted Essentially Non-oscillatory (WENO) scheme to simulate the magnetohydrodynamic (MHD) effects of conductivity models on hypersonic flows of high temperature air in thermodynamic equilibrium in the low magnetic Reynolds number approximation. The same physical effects that have already been found by the authors cited above were observed. In addition, it has been numerically shown that the application of magnetic fields of moderate strengths may be able to cause significant magnetohydrodynamic drag force comparable to the aerodynamic drag force for a blunt body with the characteristic size of a meter although a blunt body with a small size requires a strong magnetic field to be applied.

It was observed that in spite of its complicated flow structure the effects on the change of shock stand-off distance and the magnetohydrodynamic drag force are proportional to the magnetic interaction parameter and inverse-proportional to the exponent of the power-law-onset model. Hence, these magnetohydrodynamic effects can be formulated in terms of these two parameters.

Comparisons of different powers for the power-law-onset models show that the effect of applied magnetic field on the shock stand-off distance is flattened as the interaction parameter increases for powers higher than 1. The power-law-onset model with two different onset temperatures shows similar efficacy of applied magnetic field on the shock stand-off distance up to a certain magnetic interaction, however the magnetohydrodynamic drag force is predicted to be much smaller if the onset temperature is higher.

It is also shown that it is more efficient to apply the magnetic field at higher altitude to change shock stand-off distance as well as to increase the ratio of magnetohydrodynamic drag force to aerodynamic drag force in cases of 40km and 60km. Therefore, it is important to optimize the magnetohydrodynamic flow control by considering various altitudes and flow speeds.

The power-law-onset electrical conductivity model is a simple model to study various effect of applied magnetic field on low magnetic Reynolds number magnetohydrodynamic flows and it can reveal many interesting features of magnetohydrodynamic flow control. However, due to its simplicity, better electrical conductivity models are to be used for further study. Also, computations for nonequilibrium flows, that require the use of chemical reaction kinetic equations, are needed to study various flight trajectories and speed regimes.

Chapter 12

Future Work

Hypersonic flows show many different aspects depending on the altitude and the speed. As a result, a good numerical solver for hypersonic flows is desired to have many additional features and, at the same time, better robustness.

1) To make the numerical solver work better for broader range of applications it is indispensable to incorporate the chemical reactions and even radiation processes to account for the nonequilibrium phenomena.

2) A very thorough grid study is required to assess and enhance the performance of the solver for various flow conditions.

3) A systematic comparison study between the full MHD system, which requires a different code that advances the magnetic field, and the low magnetic Reynolds number approximation, is needed to avoid improper implications by either numerical results.

4) A study of different magnetic field configurations can be done to reveal more efficient MHD flow control.

Appendix A: Publications

Journal Papers

1. J. Lee, M. Huerta, and G.C. Zha, "3D MHD Hypersonic Equilibrium Air Flow Around A Blunt Body Using High Order WENO Schemes", *Journal of Spacecraft and Rockets*, 2011 (submitted)

Conference Papers

1. J. Lee, M. Huerta, and G.C. Zha, "Hypersonic 3-D Blunt Body Equilibrium Air Flow Using High Order WENO Schemes II", AIAA-2011-0903, 49th AIAA Aerospace Sciences Meeting, Jan. 2011, Orlando, FL.

2. J. Lee, M. Huerta, and G.C. Zha, "Hypersonic 3-D Blunt Body Equilibrium Air Flow Using High Order WENO Schemes", AIAA-2010-4765, 41st Plasmadynamics and Lasers Conference, Jun. 2010, Chicago, IL.

3. J. Lee, M. Huerta, and G.C. Zha, "Low Rem 3D MHD Hypersonic Equilibrium Flow Using High-Order WENO Schemes", AIAA-2010-0229, 48th AIAA Aerospace Sciences Meeting, Jan. 2010, Orlando, FL.

4. J. Lee, M. Huerta, and G.C. Zha, "3D Steady Hypersonic Laminar MHD Flow Using High Order WENO Schemes", AIAA-2009-3913, 40th AIAA Plasmadynamics and Lasers Conference, Jun. 2009, San Antonio, TX.

5. J. Lee, M. Huerta, and G.C. Zha, "Low Magnetic Reynolds Number Hypersonic MHD Flow Using High Order WENO Schemes", AIAA-2009-0459, 47th AIAA Aerospace Sciences Meeting, Jan. 2009, Orlando, FL.

References

[1] Zha, G., Shen, Y., and B. Wang, B., "Calculation of Transonic Flows Using WENO Method with a Low Diffusion E-CUSP Upwind Scheme," 46th AIAA Aerospace Sciences Meeting, Reno, NV, January 2008.

[2] Zha, G. C., Shen, Y. Q., and Wang, B. Y., "An Improved Low Diffusion E-CUSP Upwind Scheme," *Computers and Fluids*, Vol. 48, No. 1, 2011, pp. 214–220.

[3] Shen, Y.-Q., Zha, G.-C., and Wang, B.-Y., "Improvement of Stability and Accuracy for Weighted Essentially Nonoscillatory Scheme," *AIAA Journal*, Vol. 47, No.2, 2009, pp. 331–344.

[4] Hu, Z., "Parallel Computation of Fluid-Structure Interaction Using High Resolution Upwind Schemes," Ph.D. Thesis, University of Miami, May 2005.

[5] Bertin, J. J., *Hypersonic Aerothermodynamics*, AIAA Inc., Washington D.C., 1994.

[6] Hirschel, E. H., "Viscous Effects," In Space Course, February.

[7] Hansen, C. F. and Heims, S. P., "A Review of Thermodynamic, Transport, and Chemical Reaction Rate Properties of High Temperature Air," July 1958.

[8] Bush, W. B., "Magnetohydrodynamic - Hypersonic Flow Past a Blunt Body," *Journal of the Aero/Space Sciences*, Vol. 25, November 1958, pp. 685–690, 728.

[9] Wu, C. S., "Hypersonic Viscous Flow Near the Stagnation Point in the Presence of a Magnetic Field," *Journal of the Aero/Space Sciences*, Vol. 27, December, pp. 882–893, 950.

[10] Chuskin, P. I., "Magnetized Blunt Bodies in a Hypersonic Gas Flow," *MHD*, Vol. 1, No. 3, July-September 1965, pp. 49, 55.

[11] Porter, R. W., "Theoretical Aspects of Blunt Body Magnetoaerodynamics," Ph.D. Dissertation, 1966.

[12] Ziemer, R. W., "Experimental Investigations in Magnetoaerodynamics," *Journal of the American Rocket Society*, Vol. 29, No. 9, pp. 642.

[13] Seeman, G. R. and Cambel, A. B., "Observations Concerning Magnetoaerodynamic Drag and Shock Standoff Distance," Proceedings of the National Academy of Sciences, March 1966.

[14] Nowak, R. J., Kranc, S., Porter, R. W., Yuen, M. C., and Cambel, A. B., "Magnetogasdynamic Re-Entry Phenomena," *Journal of Spacecraft and Rockets*, Vol. 4, No. 11, December 1967, pp. 1538–1542.

[15] Kranc, S., Yuen, M. C., and Cambel, A. B., "Experimental Investigation of Magnetoaerodynamic Flow Around Blunt Bodies," NASA Contractor Report, August 1969.

[16] Zeigarnik, V. A., Bityurin, V. A., and Kuranov, A. L., "On a Perspective of MHD Technology in Aerospace Applications," 1996.

[17] Bityurin, V. A., Lineberry, J. T., Potebnia, V. G., Alferov, V. I., Kuranov, A. L., and Sheikin, E. G., 1997.

[18] Hoffmann, K. A., Damevin, H. M., and Dietiker, J., "Numerical Simulation of Hypersonic Number Magnetofluiddynamic Flows," 2000.

[19] Damevin, H. M. and Hoffmann, K. A., "Numerical Simulations of Hypersonic Magnetogasdynamic Flows Over Blunt Bodies," 2002.

[20] Khan, O. U., Hoffmann, K. A., and Dietiker, J., "Validity of Low Magnetic Reynolds Number Formulation of Magnetofluiddynamics," 2007.

[21] Gaitonde, D. V. and Poggie, J., "Simulation of Magnetogasdynamic Flow Control Techniques," .

[22] Fujino, T. and Ishikawa, M., "Numerical Simulation of Control of Plasma Flow with Magnetic Field for Thermal Protection in Earth Reentry Flight," *IEEE Transactions on Plasma Science*, Vol. 34, No. 2, April 2007.

[23] Yoshino, T., Fujino, T., and Ishikawa, M., "Numerical Analysis of Reentry Trajectory Coupled with MHD Flow Control," 2007.

[24] Bityurin, V. A., Bocharov, A. N., and Lineberry, J. T., "MHD Flow Control in Hypersonic Flight," 2005.

[25] Bityurin, V. A. and Bocharov, A. N., "Effects of MHD Interaction in Reentry Flight," 2006.

[26] MacCormack, R. W., "Simulation of Hypersonic Flow within a Strong Magnetic Field," 2007.

[27] Fujino, T., Kon, S., and Ishikawa, M., "Preliminary Analysis of Electric Power Extraction by MHD Technology in Reentry Flight," 2007.

[28] MacCormack, R. W., "Flow Simulations within Strong Magnetic Fields," 2008.

[29] Sutton, B. W. and Sherman, A., McGraw-Hill Inc., New York, 1965.

[30] Bisek, N., Boyd, I. D., and Poggie, J., "Numerical Flow of Magnetohydrodynmic Flow Around a Hemisphere," 2010.

[31] Srinivasan, S., Tannehill, J., , and Weilmuenster, K., "Simplified Curve Fits for the Thermodynamic Properties of Equilibrium Air," Tech. Rep. ISU-ERI-Ames-86401 (Grant NAG-1-313), Engineering research Inst., Iowa State Univ., June 1986.

[32] Srinivasan, S., Tannehill, J. C., and Weilmuenster, K. J., "Simplified Curve Fits for the Thermodynamic Properties of Equilibrium Air," NASA Reference Publication, August 1987.

[33] Baldwin, B. S. and Lomax, H., "Thin Layer Approximation and Algebraic Model for Separated Turbulent Flows," January 1978.

[34] Knight, D., Zhou, G., Okong'o, N., and Shukla, V., "Compressible Large Eddy Simulation Using Unstructured Grids," AIAA Paper 98-0535, 1998.

[35] Wang, B. Y., "Detached-eddy Simulation of Flow Non-Linearity of Fluid-Structural Interactions using High Order Schemes and Parallel Computation," Ph.D. Thesis, University of Miami, May 2009.

[36] Wang, B.-Y. and Zha, G.-C., "Comparison of a Low Diffusion E-CUSP and the Roe Scheme for RANS Calculation," AIAA Paper 2008-0596, 46th AIAA Aerospace Sciences Meeting and Exhibit, Jan. 7-10, 2008.

[37] Jameson, A., "Time Dependent Calculations Using Multigrid with Applications to Unsteady Flows Past Airfoils and Wings," AIAA Paper 91-1596, 1991.